

On the Shape of Superbubbles Evolving in the Galactic Plane

Lorenzo Zaninetti

*Dipartimento di Fisica Generale, Via Pietro Giuria 1,
10125 Torino, Italy
zaninetti@ph.unito.it*

(Received 2003 December 4; accepted 2004 October 27)

Abstract

The galactic supershells are cavities in the interstellar medium. These shells can be explained by introducing the concept of superbubbles, the theoretical result of multiple supernova. The superbubbles can be analytically described if the ambient medium has a constant density both in the so-called bursting phase and in the subsequent adiabatic expansion. In order to solve the expansion of superbubbles in the ISM, which is a non-homogeneous medium, a numerical technique is used that divides the sphere into many sectors. By varying the time of the bursting phenomenon and the time over which the phenomenon is followed, elliptical and hour-glass shapes or vertical walls can be obtained. Application of the developed theory/code to the super-shell associated with GW 46.4+5 and with GSH 238 allows us to say that the suggested physical parameters are consistent with our theory. The map of the expanding superbubble's velocity can be tentatively traced by generating random points on the expanding surface. The structure of the galactic plane as a result of the evolution of many super-bubbles was simulated by adopting the percolation theory in order to generate new OB associations.

Key words: ISM: bubbles – ISM: clouds – Galaxy: disk – galaxies: starburst – methods: numerical

1. Introduction

The term supershell was observationally defined by Heiles (1979) where eleven HI objects were examined. The supershells have been observed as expanding shells, or holes, in the HI-column density distribution of our galaxy, in the Magellanic Clouds, in the dwarf irregular galaxy Ho-II (Puche et al. 1992), and in the nearby dwarf galaxy IC 2574 (Walter et al. 1998). The dimensions of these objects span from 100 pc to 1700 pc and often present elliptical

shapes or elongated features, which are difficult to explain based on an expansion in a uniform medium. These structures are commonly explained through introducing theoretical objects named bubble or superbubble; these are created by mechanical energy input from stars (see for example Pikel'ner 1968 ; Weaver et al. 1977). Thus, the origin of a supershell is not necessarily a superbubble, and other possible origins include collisions of high-velocity clouds (see for example Tenorio-Tagle, Bodenheimer 1988 ; Santillán et al. 1999). The worm is another observed feature that may, or may not, be associated with a wall of a superbubble. Galactic worms were first identified as irregular, vertical columns of atomic gas stretching from the galactic plane; now, similar structures are found in radio continuum and infrared maps (see for example Koo et al. (1992)).

The models that explain supershells as being due to the combined explosions of supernova in a cluster of massive stars are now briefly reviewed. Semi-analytical and hydrodynamical calculations are generally adopted. In semi-analytical calculations the thin-shell approximation can be the key to obtaining the expansion of the superbubble; see, for example, McCray 1987; McCray , Kafatos 1987; Mac Low, McCray 1988; Igumenshchev et al. 1990; Basu et al. 1999.

The thin-shell approximation has already been used in a variety of different problems, and with both analytical and numerical approaches (aside from the review by Bisnovatyi-Kogan, Silich 1995, see Begelman, Li 1992; Moreno et al. 1999). Thus the validity and limitations of the method are well known. For instance, modelling is fast and simple because only shell dynamics are included in an approximate way, while fluid variables are not included at all. The price that one has to pay is a lack of knowledge of the density and velocity profiles and, obviously, the onset and development of turbulence, instabilities or mixing cannot be followed. These facts limit the applications of this method to derive only general shapes, approximate expansion rates, and gross features of the surface mass-density distributions of the shells. A detailed comparison with the results of so-called thin-layer approximation, as described for example in Silich (1992) is now being carried out.

- The two main assumptions, which are (i) all swept-up gas accumulates infinitely in a thin shell just after the shock front and (ii) the gas pressure is uniform inside the cavity, are in common with the two models.
- The numerical equations of motion are different. For examples (1) and (5) are for during the bursting phase, and Silich's set from (5) to (9) is for the three Cartesian coordinates.
- In our model the shear due to galactic rotation is neglected in a first approximation. See subsubsection 2.7.1 for a late addition on shear.
- Our treatment includes the concept of efficiency of the simulation, equation (54), which is neglected by Silich.

Another source of comparison can be made with the 3D models of Silich et al. (1996), in which a number of processes not considered here are now included:

- Two mechanisms of mass injection into the cavity are adopted: thermal evaporation of both the cold expanding shell, and the clouds engulfed by the shell, and dynamic disruption of clouds penetrating into the bubble interior.
- A power-law density and temperature distribution inside the superbubble during the entire evolution.
- A cooling function that takes into account the metallicity gradients in the Galaxy.

However the astrophysical results of Silich et al. (1996) are basically similar to ours, and the maximum elongation of the superbubbles along the z-direction can reach 2 kpc in both models. Similar results are also obtained concerning the morphologies: in both models the hourglass-shape is obtained when equality between the bursting time and the elapsed time is assumed. The vertical walls considered here are the belt of subsection 4.2 of Silich et al. (1996).

The hydrodynamical approximation was used by MacLow et al. (1989). As for the effect of magnetic fields, a semi-analytical method was introduced by (Ferriere et al. 1991) and a magneto-hydrodynamic code has been adopted by various authors (Tomisaka 1992; Tomisaka 1998; Kamaya 1998).

The plane of the numerical analysis is now outlined.

A numerical code that solves the momentum equation coupled with the variation of pressure in the presence of the injection of mechanical luminosity and adiabatic losses was developed in section 2; testing with numerical hydro-dynamic calculation was developed in subsubsection 3.1.

The analytical “expansion law” of the superbubbles can be set up both in the bursting phase (see section 2) and in the adiabatic phase after the SN burst stops, (see subsection 2.1).

The various types of obtained shape (elliptical,egg,V, vertical and hourglass) are described in subsection 3.3.

A numerical law that describes the raising of the vertical walls is deduced in subsubsection 3.3.1.

The map of the expanding superbubble’s velocity can be tentatively traced by generating random points on the expansion surface (see subsection 4.1).

The developed theory was then applied to the supershells associated with GW 46.4+5 and GSH-238 (see subsection 4.1 and subsection 4.2, respectively).

The HI structure in the galactic plane can be tentatively simulated by using the percolation framework to trace the spiral-arm structure (see section 5 and appendix 2).

By adopting the framework of radiation coming from the layer comprised between two shells, we can deduce the center darkening law (see appendix 1).

2. The Approximation Used

In our case, the starting equation for the evolution of the superbubble (McCray 1987; McCray , Kafatos 1987) is momentum conservation applied to a pyramidal section, characterised by a solid angle, $\Delta\Omega_j$:

$$\frac{d}{dt} (\Delta M_j \dot{R}_j) = p R_j^2 \Delta\Omega_j, \quad (1)$$

where the pressure of the surrounding medium is assumed to be negligible and the mass is confined into a thin shell with mass ΔM_j . The subscript j was added here in order to note that this is not a spherically symmetric system. Due to the fact that p is uniform in the cavity of the superbubble, a summation to obtain the total volume, such as

$$V = \sum \Delta\Omega_j R_j^3 / 3, \quad (2)$$

is necessary to determine its value. The mass conservation equation for a thin shell is

$$\Delta M_j = \frac{1}{3} R_j^3 \bar{\rho}_j \Delta\Omega_j. \quad (3)$$

The pressure is enclosed in the energy conservation equation,

$$\frac{1}{\gamma - 1} \frac{d(pV)}{dt} = L - p \frac{dV}{dt}, \quad (4)$$

where $L = E_0 R_{\text{SN}} / 4\pi$ denotes the mechanical luminosity injected into a unit solid angle and $\gamma = 5/3$. Equation (4) can be expanded, obtaining

$$\frac{dp}{dt} = \frac{L(\gamma - 1)}{V} - \gamma \frac{p}{V} \frac{dV}{dt}. \quad (5)$$

Formulae (1) and (5) will be our basic equations to numerically integrate in the bursting phase. An approximation concerning the pressure can be obtained by ignoring the second term of the rhs in (4); this leads to

$$p = \frac{2E_0 R_{\text{SN}} t}{3V}, \quad (6)$$

where t is the considered time, R_{SN} the rate of supernova explosions, E_0 the energy of each supernova, and V is computed as in equation (2). On continuing to consider the case of constant density, the volume becomes:

$$V = \frac{4\pi}{3} R^3. \quad (7)$$

Equations (1) and (6) lead to

$$\frac{d}{dt} (\bar{\rho} R^3 \dot{R}) = \frac{3E_0 R_{\text{SN}} t}{2\pi} \frac{R}{R}. \quad (8)$$

$R^3 \dot{R} = AR^\alpha$ is imposed to integrate this equation. After adopting the initial condition of $R = 0$ at $t = 0$ and assuming $\bar{\rho}$ is constant irrespective of R or t , the equation on the expansion speed is obtained

$$\dot{R} = \frac{\alpha+1}{\alpha} \frac{3E_0 R_{\text{SN}}}{4\pi\bar{\rho}R^4} t^2. \quad (9)$$

By integrating the previous equation, “the expansion law” is obtained,

$$R = \left[\frac{5(\alpha+1)}{4\pi\alpha} \right]^{1/5} \left(\frac{E_0 R_{\text{SN}}}{\bar{\rho}} \right)^{1/5} t^{3/5}, \quad (10)$$

which is identical to equation (10.34) of McCray (1987), since $\alpha = 7/3$.

2.1. After SN Bursts Stop

It is clear that an upper limit should be inserted into the basic equation (6); this is the time after which the bursting phenomena stops, t^{burst} .

Since there is the $p dV$ term in the the first theorem of thermodynamics ($dQ = 0 = dU + pdV$), the total thermal energy decreases with time. The pressure of the internal gas decreases according to the adiabatic law,

$$p = p_1 \left(\frac{V_1}{V} \right)^{5/3}, \quad (11)$$

where

$$p_1 = \frac{2}{3} \frac{E_0 R_{\text{SN}} t^{\text{burst}}}{V_1}, \quad (12)$$

and the equation for the conservation of momentum becomes

$$\frac{d}{dt} \left(\bar{\rho}_j R_j^3 \dot{R}_j \right) = 3 \frac{p_1 V_1^{5/3}}{V^{5/3}} R_j^2. \quad (13)$$

It is important to remember that this phase occurs after the SN burst stops. At that time ($t = t^{\text{burst}}$), the volume of the bubble is computed by using $R_j(t^{\text{burst}})$, and the expansion speed is equal to $\dot{R}_j(t^{\text{burst}})$, both of which are obtained from the numerical solution of equation (8). On assuming (also here) that $\bar{\rho}$ is constant irrespective of R or t , equation (12) is now inserted into equation (1) and the expansion law is obtained for the after-burst phase,

$$R = \left(\frac{147}{4\pi} \right)^{1/7} \left(\frac{E_0 R_{\text{SN}} t^{\text{burst}} R_1^2}{\bar{\rho}} \right)^{1/7} t^{2/7}, \quad (14)$$

which is identical to equation (10.33) of (McCray 1987).

2.2. Numerical Integration

The differential equations need to be solved by sectors, with each sector being treated as independent from the others, except for the coupling in computing the volume [see equation (2)] of the bubble. From a practical point of view, the range of the polar angle θ (180°) will be divided into n_θ steps, and the range of the azimuthal angle ϕ (360°) into n_ϕ steps. This will yield $(n_\theta + 1) (n_\phi + 1)$ directions of motion that can also be identified with the number of vertices of the polyhedron representing the volume occupied by the expansion; this polyhedron varies from a sphere to various morphological shapes based on the swept up material in each direction.

In 3D plots showing the expansion surface of the explosion, (see for example figure 12), the number of vertices is $n_v = (n_\theta+1) \cdot (n_\phi + 1)$ and the number of faces is $n_\theta \cdot n_\phi$, typically we have $n_\theta=50$ and $n_\phi=50$ (in this case the subscript varies between 1 and 2601). However, all calculated models are axisymmetric, and the essential number of points to draw such figures is only $n_\theta + 1=51$. R_{up} , R_{eq} and R_{down} are now introduced, which represent the distances from the position of the OB associations (denoted by z_{OB}) to the top, to the left and to the bottom of the bubble; see, for example, figure 2 where $z_{\text{OB}} = 100$ pc.

2.3. The Numerical Equations

At each time step Δt , the volume V of the expanding bubble is computed [see equation (2)]. In other words, the volume V swept up from the explosions is no longer a sphere, but becomes an egg or an hourglass. The pressure in the first phase, see equation (5), is computed through the following finite-difference approximation:

$$p^k = p^{k-1} + \left[L \frac{\gamma - 1}{V^k} - \gamma \frac{p^{k-1} V^k - V^{k-1}}{V^k} \frac{V^k - V^{k-1}}{\Delta t} \right] \Delta t, \quad (15)$$

where k is the number of steps considered.

Equation (1) now leads to

$$\frac{d}{dt} \left(\bar{\rho}_j R_j^3 \dot{R}_j \right) = 3p R_j^2, \quad (16)$$

which may be rewritten as

$$3R_j^2 \dot{R}_j^2 + R_j^3 \ddot{R}_j = 3p \frac{R_j^2}{\bar{\rho}_j} - \frac{\dot{\bar{\rho}}_j}{\bar{\rho}_j} R_j^3 \dot{R}_j. \quad (17)$$

The first term represents the ram pressure of the stratified ISM on the expanding surface and the second represents the inertia of the bubble. The average density $\bar{\rho}_j$ is numerically computed according to the algorithm outlined in subsection 2.5; the time derivative of $\bar{\rho}_j$ at each time step Δt is computed according to the finite difference-approximation,

$$\dot{\bar{\rho}}_j = \frac{\bar{\rho}_j^k - \bar{\rho}_j^{k-1}}{\Delta t}, \quad (18)$$

where k is the number of steps considered.

Equation (17) can be re-expressed in two differential equations (along each direction j) of the first order suitable to be integrated:

$$\frac{dy_{1,j}}{dt} = y_{2,j}, \quad (19)$$

$$\frac{dy_{2,j}}{dt} = 3p \frac{1}{\bar{\rho}_j y_{1,j}} - 3 \frac{y_{2,j}^2}{y_{1,j}} - \frac{\dot{\bar{\rho}}_j}{\bar{\rho}_j} y_{2,j}. \quad (20)$$

In the new regime ($t \geq t^{\text{burst}}$) equation (13) now becomes

$$3R_j^2 \dot{R}_j^2 + R_j^3 \ddot{R}_j = 3 \frac{p_1 V_1^{5/3}}{V_1^{5/3} \bar{\rho}_j} R_j^2 - \frac{\dot{\bar{\rho}}_j}{\bar{\rho}_j} R_j^3 \dot{R}_j. \quad (21)$$

Equation (21) can be re-expressed as two differential equations (along each direction j) of the first order suitable to be integrated:

$$\frac{dy_{1,j}}{dt} = y_{2,j}, \quad (22)$$

$$\frac{dy_{2,j}}{dt} = \frac{3p_1V_1^{5/3}}{V^{5/3}\bar{\rho}_jy_{1,j}} - 3\frac{y_{2,j}^2}{y_{1,j}} - \frac{\dot{\bar{\rho}}_j}{\bar{\rho}_j}y_{2,j}. \quad (23)$$

The integrating scheme used is a Runge-Kutta method, and in particular the subroutine RK4 (Press et al. 1992); the time derivative of the density along a certain direction j , $\dot{\bar{\rho}}_j$, is computed at each time step according to formula (18).

The integration time, t_{age} , and the time steps are always indicated in the captions connected with the various diagrams.

From a numerical point of view, the pressure across the bursting time is continuous. This is because the first value of the pressure after the bursting time is that of the last step in the bursting phase, modified according to the adiabatic law modelled by formula (11).

The upper limit chosen to integrate the differential equations is $t_{\text{age}} = 2.5 \cdot 10^7$ yr; this is the approximate age of GSH 238, the super-shell simulated in subsection 4.2.

2.4. The Density Profile

The vertical density distribution of galactic HI is well-known; specifically, it has the following three component behaviour as a function of z , the distance from the galactic plane in pc:

$$n(z) = n_1 e^{-z^2/H_1^2} + n_2 e^{-z^2/H_2^2} + n_3 e^{-|z|/H_3}. \quad (24)$$

We took (Bisnovatyi-Kogan, Silich 1995; Dickey, Lockman 1990; Lockman 1984) $n_1=0.395$ particles cm $^{-3}$, $H_1=127$ pc, $n_2=0.107$ particles cm $^{-3}$, $H_2=318$ pc, $n_3=0.064$ particles cm $^{-3}$, and $H_3=403$ pc. This distribution of galactic HI is valid in the range $0.4 \leq R \leq R_0$, where $R_0 = 8.5$ kpc and R is the distance from the galaxy center. A plot showing such a dependence of the ISM density from z is shown in figure 1.

2.5. Computation of the Swept Mass

The ISM density is not constant, but varies in the z -direction according to equation (24). The swept mass can therefore be computed in a certain direction j using the following algorithm:

1. The pyramidal sector is divided into layers (for example 1000) whose radii range from $R_{L-1/2}$ to $R_{L+1/2}$.
2. In each layer the volume $\Delta V_L = \frac{1}{3}(R_{L+1/2}^3 - R_{L-1/2}^3)$ is computed as well as the corresponding mass, $\Delta M_L = \Delta V_L \rho_j(z = R_L \cos \theta_j + z_{\text{OB}})$, where θ_j represents an angle between the z -axis and the j -th radial path.
3. The various contributions, ΔM_L , are added in order to obtain the total swept mass in the considered sector.

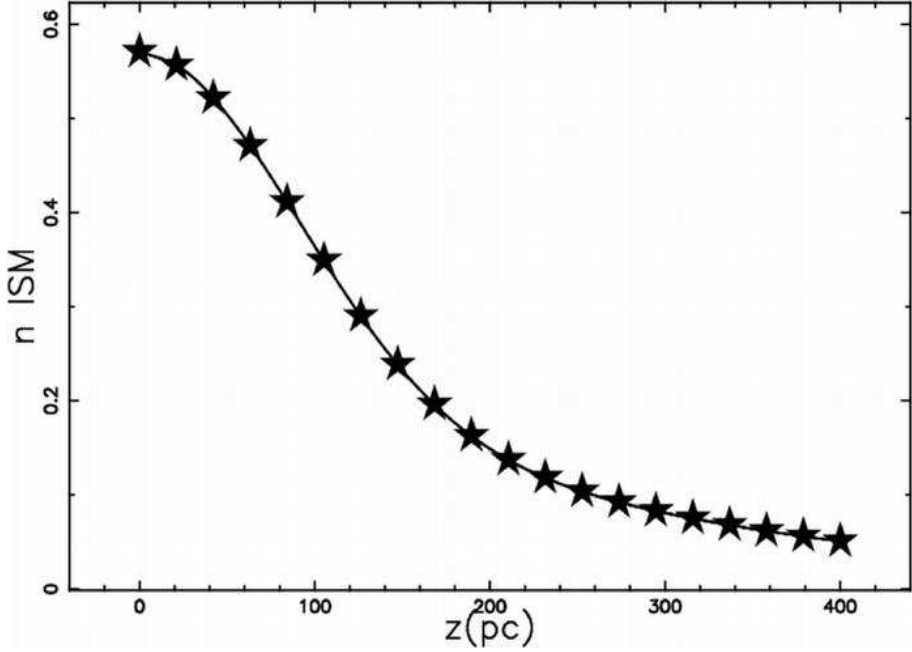


Fig. 1. Average structure of the gaseous disk in the z -direction; z is allowed to vary between 0 pc and 400 pc.

4. The average density along a sector j as $\bar{\rho}_j$ is calculated using ΔM_L and ΔV_L as $\bar{\rho}_j = \sum_L \Delta M_L / \sum_L \Delta V_L$.

2.6. Astrophysical Units

Our basic units are: time (t_7), which is expressed in 10^7 yr units; E_{51} , the energy in 10^{51} erg; n_0 the density expressed in particles cm^{-3} (density $\rho_0 = n_0 m$, where $m = 1.4 m_H$); and N^* , which is the number of SN explosions in $5.0 \cdot 10^7$ yr.

By using the previously defined units, formula (10) concerning “the expansion law” in the bursting phase becomes

$$R = 111.56 \text{ pc} \left(\frac{E_{51} t_7^3 N^*}{n_0} \right)^{\frac{1}{5}}. \quad (25)$$

Conversely, equation (14) concerning “the expansion law” in the adiabatic phase is

$$R = 171.85 \text{ pc} \left(\frac{E_{51} N^*}{n_0} \right)^{\frac{1}{5}} (t_7^{\text{burst}})^{\frac{11}{35}} (t_7)^{\frac{2}{7}}. \quad (26)$$

This is the approximated radius derived by a spherical model. A perfect coincidence is not expected upon making a comparison with that expected in a stratified medium obtained with the multidimensional thin shell approximation. Another useful formula is the luminosity of the bubble (see McCray 1987),

$$L_{\text{SN}} = E_0 R_{\text{SN}} = 0.645^{36} \text{ erg s}^{-1} E_{51} N^*. \quad (27)$$

This formula can be useful in order to derive the parameter N^* based on observations; for

example, a luminosity of $1.6 \cdot 10^{38} \text{ erg s}^{-1}$ corresponds to $N^* = 248$. The total deposited energy, E_{tot} , is

$$E_{\text{tot}} = E_{51} N^* 10^{51} \frac{t_{\text{age}}}{5 \cdot 10^7 \text{ yr}} \text{ erg}, \quad (28)$$

when $t^{\text{burst}} = t_{\text{age}}$ and

$$E_{\text{tot}} = E_{51} N^* 10^{51} \frac{t^{\text{burst}}}{5 \cdot 10^7 \text{ yr}} \text{ erg}, \quad (29)$$

when $t^{\text{burst}} < t_{\text{age}}$.

The spectrum of the radiation emitted depends on the temperature behind the shock front [see for example formula 9.14 in McKee (1987)],

$$T = \frac{3}{16} \frac{\mu}{k} v_s^2 \text{ K}^\circ, \quad (30)$$

where μ is the mean mass per particle, k the Boltzmann constant and v_s the shock velocity expressed in cm sec^{-1} . A formula which is useful for the implementation in the code is easily derived,

$$T = 31.80 v_{\text{sk}}^2 \text{ K}^\circ, \quad (31)$$

when v_{sk} is expressed in km sec^{-1} .

2.7. Other Effects

Two other effects are now analysed: the galactic rotation and the influence of the ambient pressure on the late phase of motion.

2.7.1. Galactic Rotation

The effects of galactic rotation are important in shaping the bubbles, as can be seen in figure 2 of Silich et al. (1996). This is very important on the galactic plane, and the properties of the distorted "walls" for a rotating galaxy were described by Palous et al. (1990). The application of this distortion to Gould's Belt was done by Moreno et al. (1999), and the impact on large scales in a percolation-type scheme (in this case the cloud and star-formation mechanism is deterministic, not stochastic) was studied by Palous et al (1994). The distortion of the superbubble due to galactic rotation is now introduced. The rotation curve can be that given by Wouterloot et al. (1990),

$$V_R(R_0) = 220 \left(\frac{R_0 [\text{pc}]}{8500} \right)^{0.382} \text{ km sec}^{-1}, \quad (32)$$

where R_0 is the radial distance from the center of the Galaxy expressed in pc. The translation of the previous formula to the astrophysical units adopted gives

$$V_R(R_0) = 2244 \left(\frac{R_0 [\text{pc}]}{8500} \right)^{0.382} \frac{\text{pc}}{10^7 \text{ yr}}, \quad (33)$$

$$\Omega(R_0) = 2244 \frac{\left(\frac{R_0[\text{pc}]}{8500}\right)^{0.382}}{R_0[\text{pc}]} \frac{\text{rad}}{10^7 \text{ yr}}. \quad (34)$$

Here, $\Omega(R_0)$ is the differential angular velocity and

$$\phi = 2244 \frac{\left(\frac{R_0[\text{pc}]}{8500}\right)^{0.382}}{R_0[\text{pc}]} t_7 \text{ rad.} \quad (35)$$

Here, ϕ , is the angle made on the circle and t_7 the time expressed in 10^7 yr units. Upon considering only a single object, an expression for the angle can be found once $R = R_0 + y$ is introduced,

$$\phi(y) = \frac{V_R(R_0)}{R_0 + y} t. \quad (36)$$

The shift in the angle due to differential rotation can now be introduced,

$$\Delta\phi = \phi(y) - \phi(0), \quad (37)$$

where x and y are the superbubble coordinates in the inertial frame of the explosion, denoted by $x=0, y=0$ and $z=z_{\text{OB}}$. The great distance from the center allows us to say that

$$\frac{\Delta x}{R_0} = \Delta\phi, \quad (38)$$

where Δx is the shift due to the differential rotation in the x coordinate. The shift can be found from (38) and (37) once a Taylor expansion is performed,

$$\Delta x \approx -V_R(R_0) \frac{y}{R_0} t. \quad (39)$$

Upon inserting (33) in (39), the following transformation, T_r , due to the rotation is obtained for a single object in the solar surroundings:

$$T_r \begin{cases} x' = x + 0.264y t \\ y' = y \\ z' = z, \end{cases} \quad (40)$$

where y is expressed in pc and t in 10^7 yr units. A typical distortion introduced on a circular section of the superbubble, $z = z_{\text{OB}}$, is shown in figure 18.

2.8. Late Evolutionary State

The problem of the late evolutionary stages can be attached including the ambient pressure; but firstly the Euler number (ratio of the pressure forces to the inertial forces in a flow) should be introduced

$$Eu = \frac{p}{\rho_s v_s^2}, \quad (41)$$

where ρ_s is the density behind the shock, v_s is the shock velocity and p the ambient pressure. The nominal value of pressure at the Solar circle, 10^{-12} dyne cm $^{-2}$, can be used as an adequate value (see Boulares, Cox 1990). Another density distribution along the z-axis and a discussion

of the pressure distribution can be found in Kim et al. (2000). In order to simulate the influence of the ambient pressure, a drag acceleration should be introduced,

$$\frac{dy_{2,j}}{dt} = -v_d Eu, \quad (42)$$

where v_d is an artificial coefficient. This effect is negligible when the Euler number is small (high shock velocities), and gives a negative contribution when the Euler number ≈ 1 . Only in subsection 4.1 are some results adopting the value of $v_d = 6000 \text{pc}/10^7 \text{yr} \approx 600 \text{km sec}^{-1}$ reported in comparison with the normal run, the associated note "with the Euler process" being always inserted.

3. Test Calculation

The shape of the superbubble depends strongly on the time elapsed since the first explosion, t_{age} , the duration of SN burst, t^{burst} , on the number of SN explosions in the bursting phase, and on the adopted density profile.

In this section, where the initial tests are discussed the galactic rotation is neglected.

Ordinarily, the dynamics of a superbubble is studied with hydro simulations (partial differential equations). Conversely, here under the hypothesis called "thin-shell approximation", the dynamics is studied by solving ordinary differential equations. This choice allows the calculation of a much larger number of models compared with hydro-dynamics calculations.

3.1. Reliability of the code

The level of confidence in our results can be given by a comparison with numerical hydro-dynamics calculations see, for example, MacLow et al. (1989). The vertical density distribution they adopted [see equation(1) from MacLow et al. (1989) and equation(5) from Tomisaka, Ikeuchi (1986)] has the following it z dependence, the distance from the galactic plane in pc:

$$n_{\text{hydro}} = n_d \left\{ \Theta \exp \left[-\frac{V(z)}{\sigma_{\text{IC}}^2} \right] + (1 - \Theta) \exp \left[-\frac{V(z)}{\sigma_{\text{C}}^2} \right] \right\}, \quad (43)$$

with the gravitational potential as

$$V(z) = 68.6 \ln \left[1 + 0.9565 \sinh^2 \left(0.758 \frac{z}{z_0} \right) \right] (\text{km s}^{-1})^2. \quad (44)$$

Here $n_d = 1 \text{ particles cm}^{-3}$, $\Theta = 0.22$, $\sigma_{\text{IC}} = 14.4 \text{km s}^{-1}$, $\sigma_{\text{C}} = 7.1 \text{km s}^{-1}$ and $z_0 = 124 \text{ pc}$. Table 1 reports the results of ZEUS (see MacLow et al. 1989), a two-dimensional hydrodynamic code, when $t_{\text{age}} = 0.45 \cdot 10^7 \text{ yr}$. The supernova luminosity is $1.6 \cdot 10^{38} \text{erg s}^{-1}$, $z_{\text{OB}} = 100 \text{ pc}$ and the density distribution is given by formula (43). The ZEUS code was originally described by Stone, Norman (1992).

In order to make a comparison our code was run with the parameters of the hydro-code (see figure 2); a density profile as given by formula (43) was adopted.

From a practical point of view, the percentage of reliability of our code can also be

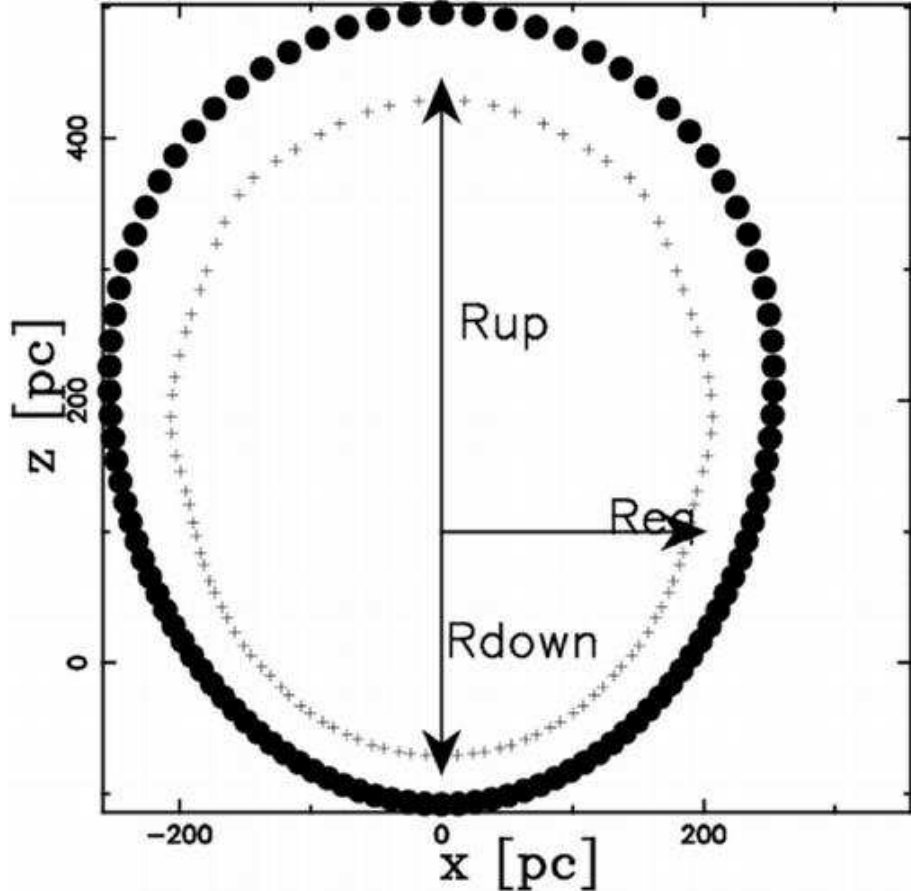


Fig. 2. Section of the superbubble on the x - z plane when the explosion starts at $z_{\text{OB}} = 100\text{pc}$. The density law is given by equation 43. The code parameters are $t_{\text{age}} = 0.45 \cdot 10^7 \text{ yr}$, $\Delta t = 0.001 \cdot 10^7 \text{ yr}$, $t_7^{\text{burst}} = 0.45$, and $N^* = 248$. The points represented by the small crosses indicate the inner section from figure 3a of MacLow et al. (1989).

introduced,

$$\epsilon = \left(1 - \frac{|(R_{\text{hydro}} - R_{\text{num}})|}{R_{\text{hydro}}}\right) \cdot 100, \quad (45)$$

where R_{hydro} is the radius, as given by the hydro-dynamics, and R_{num} the radius obtained from our simulation. In the already cited table 1, our numerical radii can also be found in the upward, downward and equatorial directions, and the efficiency as given by formula (45). The value of the radii are comparable in all of the three chosen directions. figure 2 also reports on the data from figure 3a of MacLow et al. (1989).

Koo, McKee (1990) applied their one-dimensional method based on the virial theorem to a two-dimensional calculation by using a sector approximation, which is identical to that assumed in the present paper and in which a differential equation is solved along a radial path. figure 8 from (Koo, McKee 1990) is for the same density distribution as given by formula (43).

Table 1. Code reliability.

	$R_{\text{up}}(\text{pc})$	$R_{\text{down}}(\text{pc})$	$R_{\text{eq}}(\text{pc})$
$R_{\text{hydro}}(ZEUS)$	330	176	198
$R_{\text{num}}(\text{our code})$	395	207	237
efficiency(%)	80	81	80

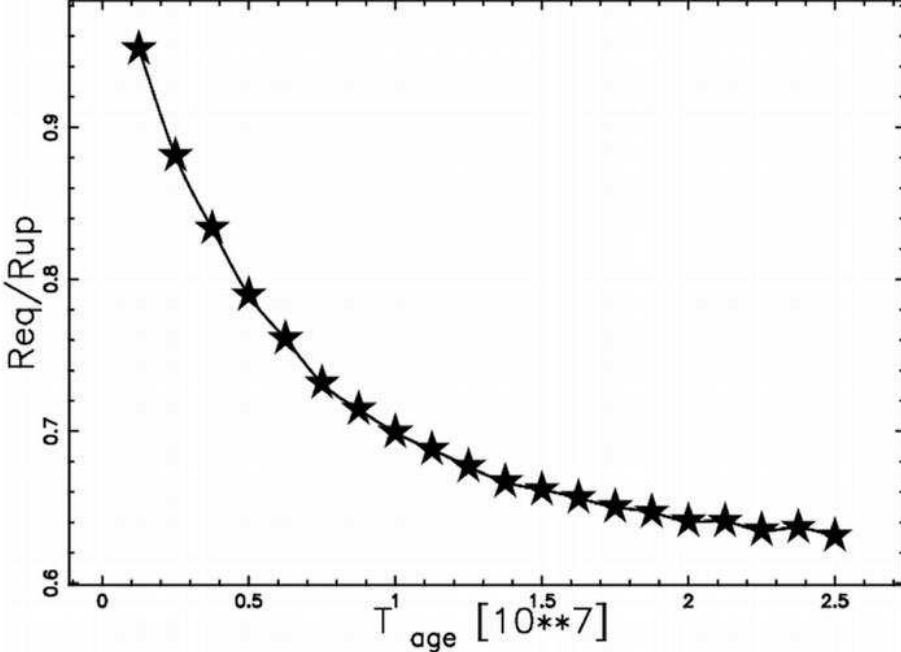


Fig. 3. $R_{\text{eq}}/R_{\text{up}}$ versus the time, t_{age} , expressed in units of 10^7 yr when the explosion starts at $z_{\text{OB}} = 0$ pc. The parameters are $\Delta t = 0.1 \cdot 10^7$ yr, $t_7^{\text{burst}} = 0.45$, and $N^* = 248$.

3.2. The Asymmetries

Firstly, the time evolution of the ratio $R_{\text{eq}}/R_{\text{up}}$ is focused on as a function of t_{age} . figure 3 plots the asymmetry indicator, $R_{\text{eq}}/R_{\text{up}}$ for a model with $z_{\text{OB}} = 0$, $t_7^{\text{burst}} = 0.45$ and $N^* = 250$. In this case, the indicator of the asymmetry, $R_{\text{eq}}/R_{\text{up}}$ is ≈ 0.9 at $t_{\text{age}} = 0.4 \cdot 10^7$ yr, reaches a minimum at $t_{\text{age}} = 2.0 \cdot 10^7$ yr and remains nearly constant up to $t_{\text{age}} = 2.5 \cdot 10^7$ yr (see figure 3).

Secondly, we consider how the asymmetry indices, $R_{\text{down}}/R_{\text{up}}$ (figure 4) and $R_{\text{eq}}/R_{\text{up}}$ (figure 6), depend upon the height of the OB association, z_{OB} . A comparison is made at $t_{\text{age}} = 4.5 \cdot 10^6$ yr and $N^* = 248$. Now, the first index of the asymmetry, $R_{\text{down}}/R_{\text{up}}$, is 1 at $z_{\text{OB}}=0$ pc and 0.52 at $z_{\text{OB}}=100$ pc (value of z_{OB} where the comparison with the hydro-code was performed; see figure 4). Another interesting theoretical parameter that has an observational counterpart is the degree of symmetry with respect to the galactic plane. Upon adopting the previously developed notation, two variables, D_{up} and D_{down} , are introduced when $R_{\text{down}} > z_{\text{OB}}$:

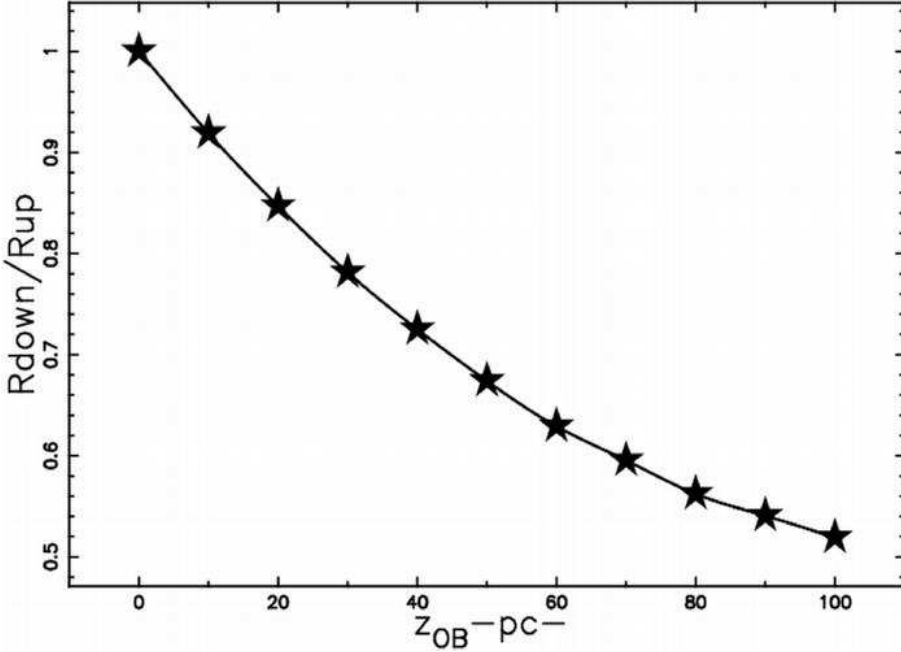


Fig. 4. $R_{\text{down}}/R_{\text{up}}$ versus z_{OB} in pc. The parameters are $t_{\text{age}}=0.45 \cdot 10^7$ yr, $\Delta t = 0.005 \cdot 10^7$ yr, $t_7^{\text{burst}}=0.45$, and $N^*=248$.

$$\begin{aligned} R_{\text{up}} + z_{\text{OB}} &= D_{\text{up}}, \\ R_{\text{down}} - z_{\text{OB}} &= D_{\text{down}}. \end{aligned} \quad (46)$$

The super-shells are often visualised in galactic coordinates. When this visualisation is possible, the ratio between the positive maximum galactic latitude and the absolute value of the negative minimum galactic latitude belonging to a given super-shell can be identified with $\frac{D_{\text{up}}}{D_{\text{down}}}$. In our theoretical framework, the ratio is easily found to be

$$\frac{D_{\text{up}}}{D_{\text{down}}} = \frac{R_{\text{up}} + z_{\text{OB}}}{R_{\text{down}} - z_{\text{OB}}}, \quad (47)$$

and can be visualised in figure 5; due to the nature of the phenomena, this ratio easily takes high values.

Conversely, the second index, $R_{\text{eq}}/R_{\text{up}}$, as a function of z_{OB} presents a marked minimum value at ≈ 100 pc; for this value of z_{OB} the asymmetry in the shape of the expanding envelope is maximum (see figure 6).

3.3. Characteristic Shapes

The developed theory of bubble expansion in the ISM has four key parameters: the distance z_{OB} from the galactic plane, t_7^{burst} , the bursting phase, N^* , the number of SN explosions in $2.5 \cdot 10^7$ yr, and t_{age} the age of the supershell. By varying these four parameters, a great variety of different shapes can be obtained and two cases, $z_{\text{OB}}=0$ pc and $z_{\text{OB}}=100$ pc, will be concentrated on.

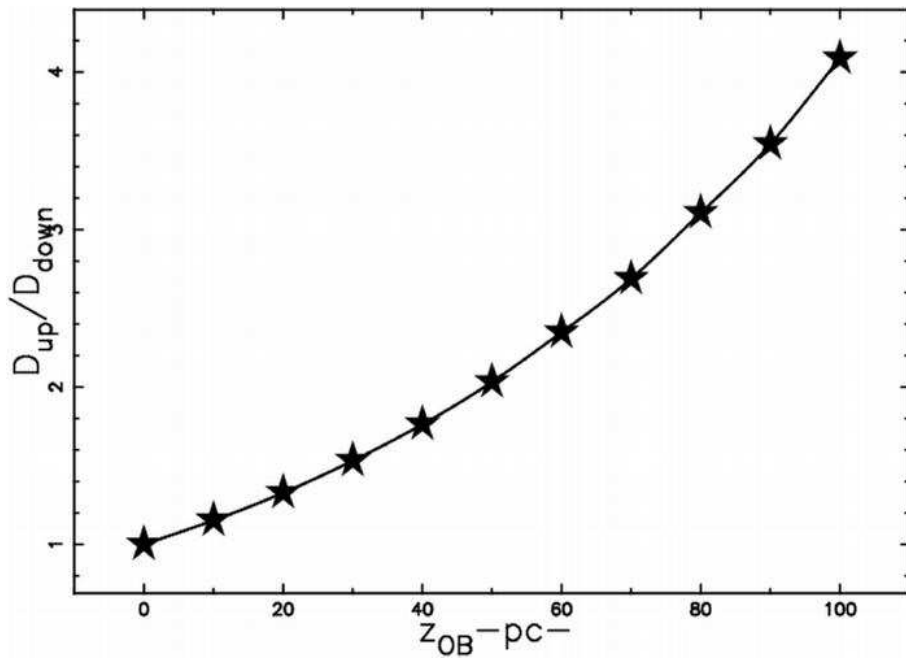


Fig. 5. Ratio $\frac{D_{\text{up}}}{D_{\text{down}}}$ versus z_{OB} in pc. The parameters are the same as in figure 4.

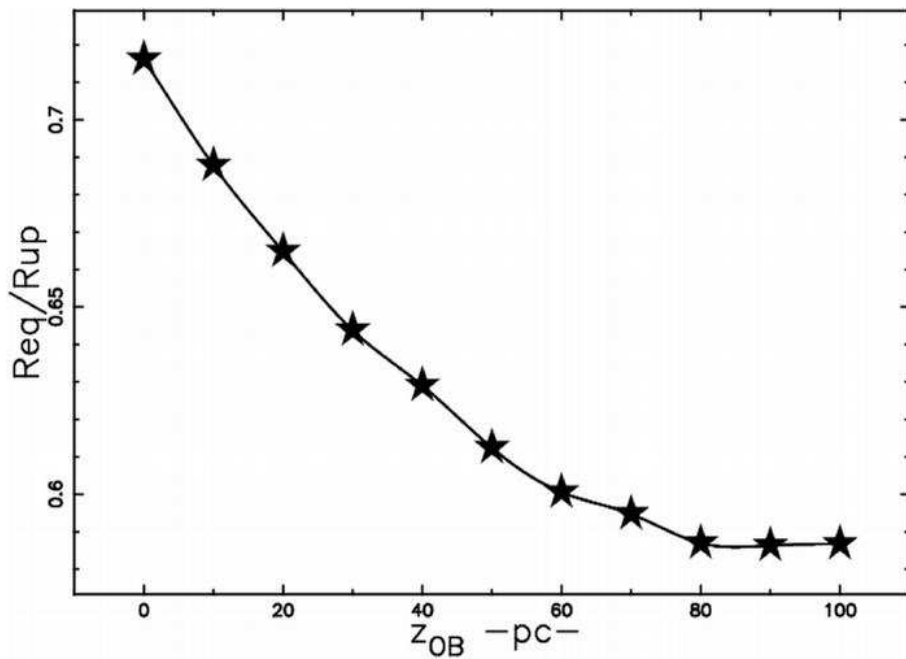


Fig. 6. $R_{\text{eq}}/R_{\text{up}}$ versus z_{OB} in pc. The physical parameters are the same as in figure 4.

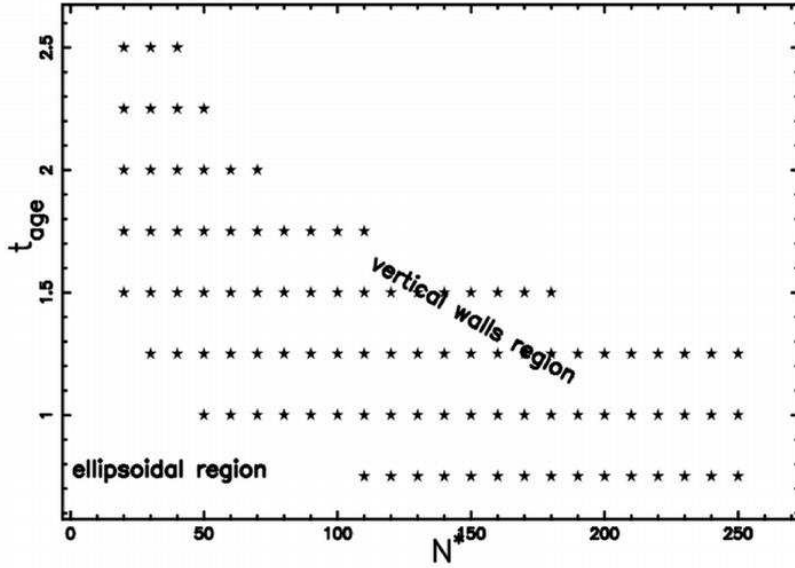


Fig. 7. Stars indicate the existence of "vertical walls"; t_{age} is expressed in 10^7yr units. The parameters are $\Delta t = 0.1 \cdot 10^7 \text{ yr}$, $z_{\text{OB}}=0$, and $t^{\text{burst}} = t_{\text{age}}$.

3.3.1. From the ellipse to the hourglass, $z_{\text{OB}}=0 \text{ pc}$

We start by fixing $z_{\text{OB}}=0 \text{ pc}$ (the symmetrical case in the $+z$ and $-z$ directions). If the luminosity is high enough and $z_{\text{OB}} = 0$, the superbubble changes its shape from spheroidal to hourglass shape via the vertical wall. In order to define the vertical wall, a reasonable angle of 30° is first introduced between the plane $z = 0$ and a certain radius, R_{30° ; this radius projected on the $z=0$ plane is denoted by $R_{p,30^\circ}$. From this point of view, a vertical wall is made if $R_{z=0} \simeq R_{p,30^\circ}$; $R_{z=0} > R_{p,30^\circ}$ indicates the elliptical shape and $R_{z=0} < R_{p,30^\circ}$ indicates the hourglass shape. Another way to express the previous definition is the following inequality, which can be easily embedded in the code:

$$\frac{|R_{\text{eq}} - R_{p,30^\circ}|}{R_{\text{eq}}} \cdot 100 \leq 5\%. \quad (48)$$

Through such a definition, the vertical walls will span 60° on the galactic height. The existence of the vertical wall can now be plotted in the $t_{\text{age}} - N^*$ space; see figure 7 when $t^{\text{burst}} = t_{\text{age}}$, and figure 8 when $t^{\text{burst}} = 0.5$.

From these two plots (7 and 8) it can be inferred that:

- When $t_7^{\text{burst}} = 0.5$, vertical walls are only developed if $N^* \geq 20$; for example at $N^* = 100$ they appear at $t_{\text{age}} \approx 1.0 \cdot 10^7 \text{ yr}$ (see figure 8). In this case the transition from an ellipse to an hourglass is not observed; in other words, the vertical walls are the typical structure over a wide range of t_{age} and N^* .

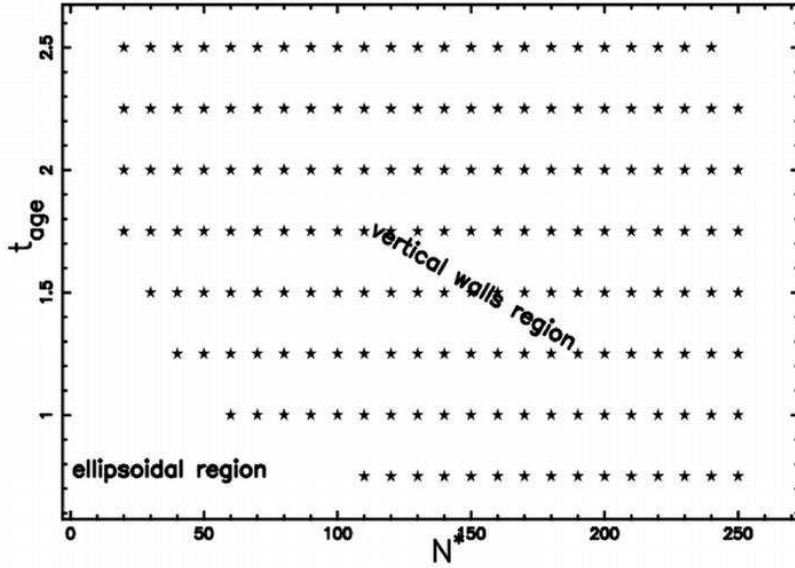


Fig. 8. Stars indicate the existence of the "vertical walls"; t_{age} is expressed in 10^7 yr units. The parameters are $\Delta t = 0.1 \cdot 10^7$ yr, $z_{\text{OB}} = 0$ pc, and $t_7^{\text{burst}} = 0.5$.

- When $t^{\text{burst}} = t_{\text{age}}$ the transition between the various zones is better defined; for example, at $N^* = 50$ the vertical walls appear at $t_{\text{age}} \approx 1.0 \cdot 10^7$ yr (see figure 7).

A typical plot showing the temporal development of vertical walls through a displacement of the sections at regular time intervals is reported in figure 9. Further on, from the data of plots (7 and 8), we can extract an approximate age, after which the vertical walls appear when $t_7^{\text{burst}} = 0.5$, $t_{\text{VW}}^{0.5}$ and when $t^{\text{burst}} = t_{\text{age}}$, $t_{\text{VW}}^{\text{age}}$. The numerical law can be obtained by fitting the value t_{VW} (the value of t_{age} at which the vertical walls appear) versus N^* ,

$$\log(t_{\text{VW}}) = a + b \cdot \log(N^*). \quad (49)$$

The values of a and b are easily derived from the least-squares fitting procedure. In other words, this relationship connects N^* and the first corresponding value of t_{age} at the left of figure 7, and figure 8 is defined as t_{VW} . The application of least-squares gives

$$t_{\text{VW}}^{0.5} = 4.5(N^*)^{-0.34} \cdot 10^7 \text{ yr}, \quad (50)$$

$$t_{\text{VW}}^{\text{age}} = 3.2(N^*)^{-0.28} \cdot 10^7 \text{ yr}. \quad (51)$$

It can therefore be concluded that introducing of a finite value of t^{burst} (for example $t_7^{\text{burst}} = 0.5$) inhibits the transition from the vertical walls to the hourglass shape. It is important to note that the time necessary to develop vertical walls decreases when the key parameter, N^* , increases; the exact law being an inverse power. In other words, the momentaneous radius of the evolving superbubble in the galactic plane ($z=0$) gives a reference radius; the balance between

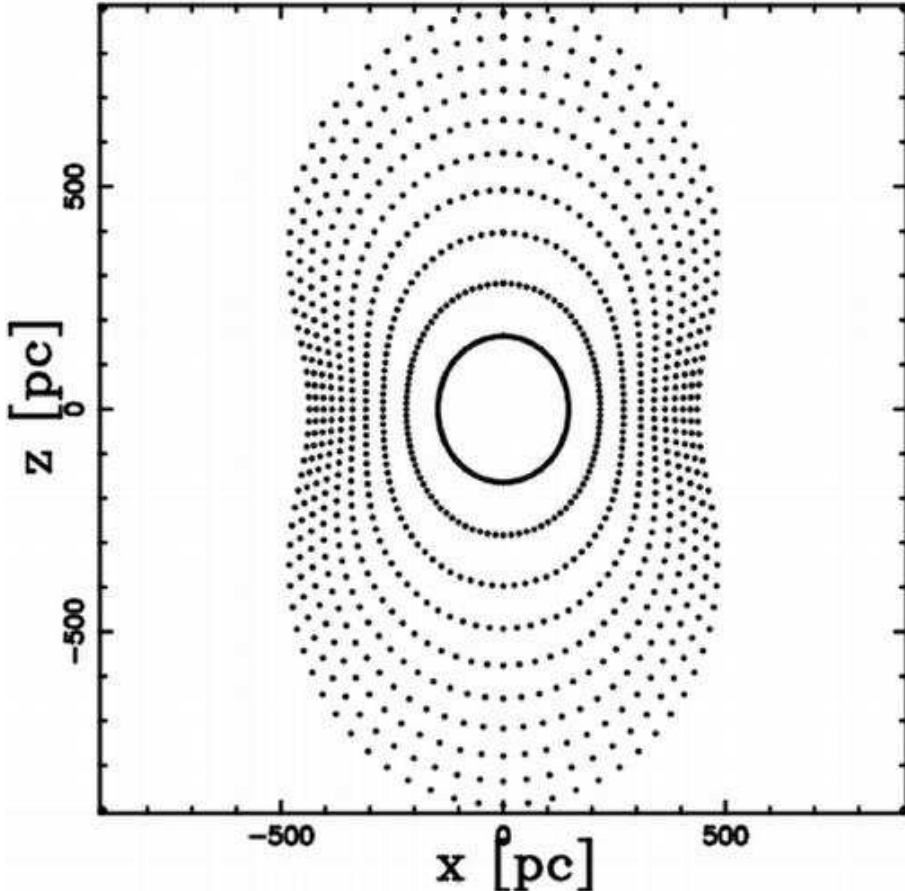


Fig. 9. Section of the superbubble on the x - z plane. The parameters are $t_{\text{age}}=2.5 \cdot 10^7$ yr, $\Delta t=0.01 \cdot 10^7$ yr, $z_{\text{OB}}=0$ pc, $t_7^{\text{burst}}=0.5$, and $N^*=100$. The sections at regular intervals of $t_{\text{age}}/10$ are also shown.

a progressively greater distance at higher values of z and the decreasing matter encountered along the trajectory allows the radius along the other directions to be greater with respect to that along the galactic plane. Under the existence of certain parameters, as given by the numerical laws (50) and (51), a progressively increasing radius (connected with the progressive angle with respect to the galactic plane) having a "vertical shape" is obtained.

3.3.2. Toward the V-shape, $z_{\text{OB}} > 0$ pc

A substantial modification of the up/down symmetry with respect to the galactic plane can be obtained by varying the distance z_{OB} from the galactic plane. In this case the morphologies become complicated and we limit ourselves to exploring the situation at $z_{\text{OB}}=100$ pc where a transition from the egg shape to the V-shape is observed (see figure 10); in this case the temporal evolution of the superbubble is visualised through a displacement of the sections at regular time intervals.

When $z_{\text{OB}}=100$ pc the density in the equatorial plane of the explosions is \approx two-times lower with respect to the density of the galactic plane. The surface of the expansion will

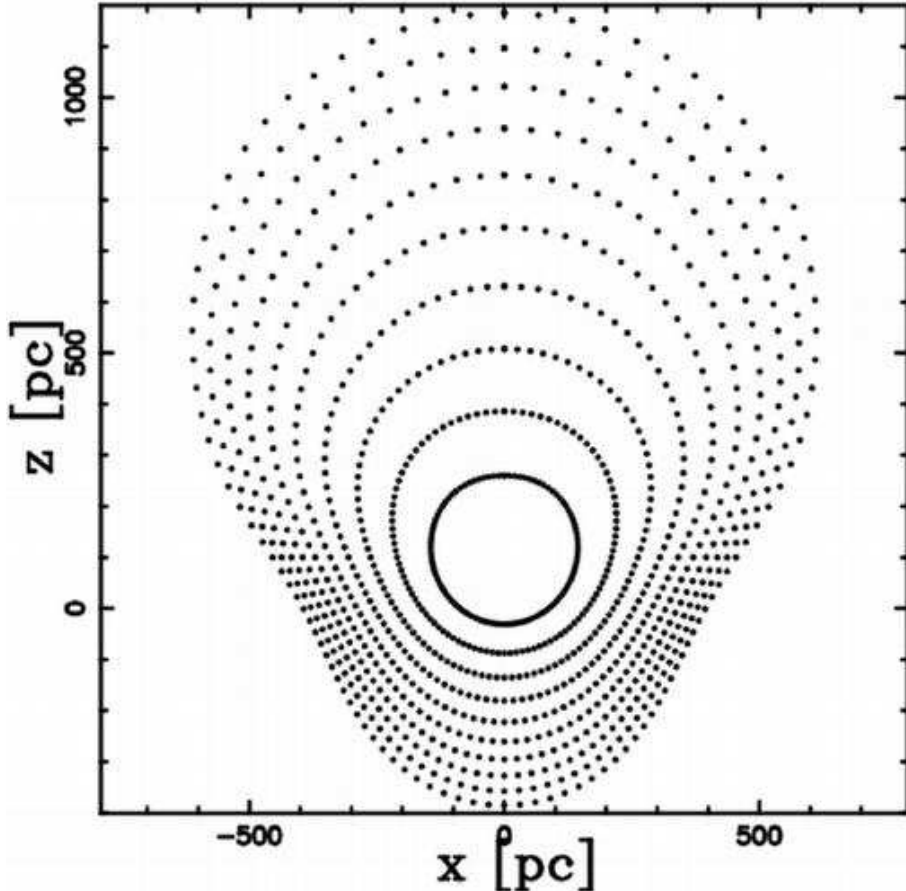


Fig. 10. Section of the superbubble on the x - z plane. The parameters are $t_{\text{age}} = 2.5 \cdot 10^7$ yr, $\Delta t = 0.01 \cdot 10^7$ yr, $z_{\text{OB}} = 100$ pc, $t_7^{\text{burst}} = 0.5$, and $N^* = 250$. The sections at regular intervals of $t_{\text{age}}/10$ are also shown.

therefore find an increasing density in the downward direction and, conversely, a decreasing density in the upward direction; the curious V-shape is generated from the competition of these two effects.

The effect of increasing the bursting time is shown in figure 11, where $t^{\text{burst}} = t_{\text{age}}$ rather than $t^{\text{burst}} = 0.5 \cdot 10^7$ yr of figure 10. In the case of figure 11, the maximum elongation along the z -direction is ≈ 1400 pc against ≈ 1100 pc of figure 10, in which a limited time of bursting was chosen.

4. Single Astrophysical Objects

Another way of detecting supershells is through a search for galactic worms; they are filamentary, vertical structures that look like worms crawling away from the galactic plane in HI and infrared surveys (60 and $100\mu\text{m}$) (Koo et al. 1992).

With respect to the worms, there are also several alternatives to their origin. A possibility is due to gravo-magnetic instabilities, such as the Parker instability in 3D, which forms worm-

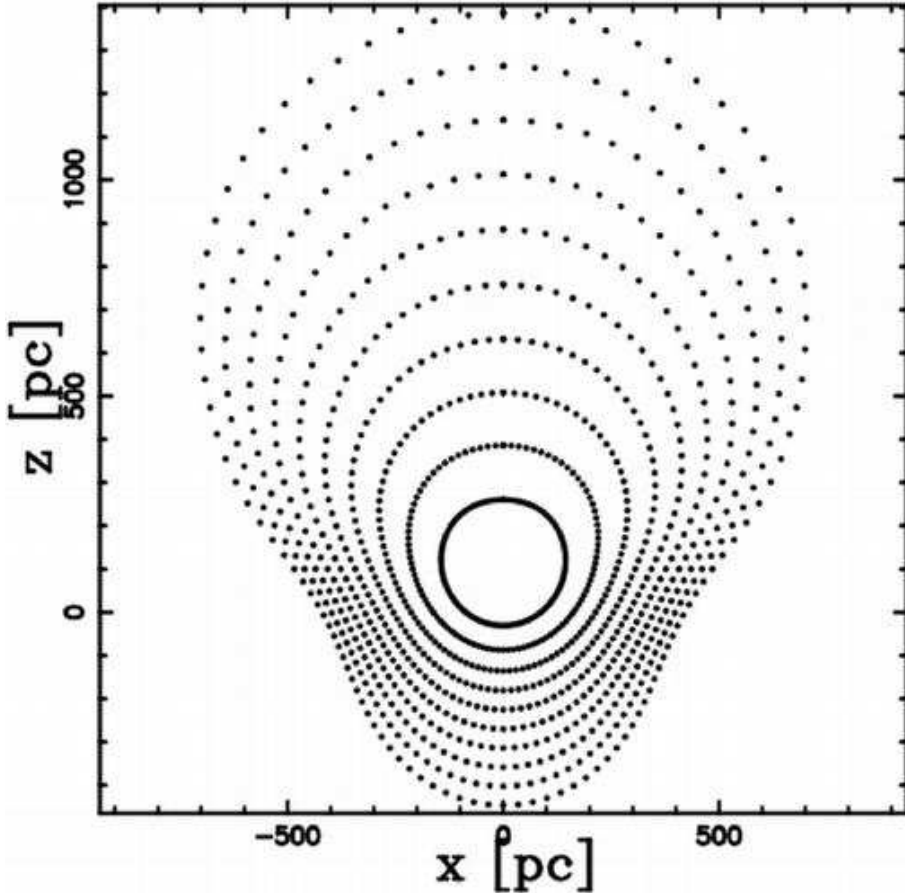


Fig. 11. Same as figure 10, but with $t^{\text{burst}} = t_{\text{age}}$.

like structures, as can be seen in figure 4b of Franco et al. 2002.

Here, it is assumed that they are the vertical walls of supershells, as sustained by an observational point of view (Kim , Koo 2000) or by a theoretical argument (see appendix 1).

The developed theory is now applied to a well-defined galactic supershell (see subsection 4.1 and subsection 4.2).

In this astrophysical section the galactic rotation is inserted.

4.1. Supershell Associated with GW 46.4+5.5

A careful study of the worms 46.4+5.5 and 39.7+5.7 (Kim , Koo 2000) has led to the conclusion that they belong to a single super-shell. Further on, the dynamical properties of this HI supershell can be deduced by coupling the observations with theoretical arguments, Igumenshchev et al. (1990); the derived model parameters to fit observations are reported in table 2, where the altitudes of KK 99 3 and KK 99 4 (clouds that are CO emitters) have been identified with z_{OB} by the author.

These parameters are the input for our computer code (see the captions of figure 12). The problem of assigning a value to z_{OB} now arises, and the following two equations are set up:

Table 2. Data of the supershell associated with GW 46.4+5.5.

Size (pc ²)	345 · 540
Expansion velocity (km s ⁻¹)	15
Age (10 ⁷ yr)	0.5
z_{OB} (pc)	100
Total energy (10 ⁵¹ erg)	15

$$\begin{aligned} R_{up} + z_{OB} &= 540, \\ \frac{R_{up} + z_{OB}}{R_{down} - z_{OB}} &= \frac{D_{up}}{D_{down}} = \frac{15^\circ}{3^\circ} = 3. \end{aligned} \quad (52)$$

The algebraic system (52) consists in two equations and three variables. The value chosen for the minimum and maximum latitude (15° and -5°) is in rough agreement with the position of the center at +5° of the galactic latitude (see Koo et al. 1992). One way of solving system 52 is to set, for example, $z_{OB}=100$ pc. The other two variables are easily found to be as follows:

$$\begin{aligned} z_{OB} &= 100 \text{ pc}, \\ R_{down} &= 235 \text{ pc}, \\ R_{up} &= 305 \text{ pc}. \end{aligned} \quad (53)$$

For this value of z_{OB} , we have the case where a transition from egg-shape to V-shape (as outlined in subsubsection 3.3.2) is going on, and the simulation gives the exact shape. In order to obtain $E_{tot} = 15 \cdot 10^{51}$ erg (see formula (29)) and $t^{burst} = 0.5 \cdot 10^7$ yr, we have inserted $N^* = 150$.

In order to test our simulation, an observational percentage of reliability is introduced that uses both the size and the shape,

$$\epsilon_{obs} = 100 \left(1 - \frac{\sum_j |R_{obs} - R_{num}|_j}{\sum_j R_{obs}} \right), \quad (54)$$

where R_{obs} is the observed radius, as deduced by using the following algorithm. The radius at regular angles from the vertical (0°, 90°, 180°) is extracted from table 2, giving the series (305 pc, 172.5 pc, 235 pc); the cubic spline theory (Press et al. 1992) is then applied to compute the various radii at progressive angles (0°, 3.6°, 7.2°,...180°), which is a series computed by adding regular steps of 180 °/n_θ. The data are extracted from the dotted ellipse visible in figure 7 of Koo et al. 1992; this ellipse represents the super-shell at $v_{LSR} = 18.5$ km sec⁻¹.

We can now compute the efficiency over 50+1 directions [formula (54)] of a section y - z when $x=0$ which turns out to be $\epsilon_{obs} = 68.4\%$ ($\epsilon_{obs} = 71.3\%$ with the Euler process); the observed and numerical radii along the three typical directions are reported in table 3. The physical parameters adopted from (Kim , Koo 2000) turn out to be consistent with our numerical code. The result of the simulation can be visualised in figure 12, or through a section on the x - z plane (see figure 13). Another important observational parameter is the HI 21 cm line emission: the

Table 3. Radii concerning GW 46.4+5.5.

Direction	$R_{\text{num}}(\text{pc})$	$R_{\text{num}}(\text{pc})$ with the Euler process	$R_{\text{obs}}(\text{pc})$
Equatorial	238	233	172.5
Polar up	342	335	305
Polar down	312	304	235

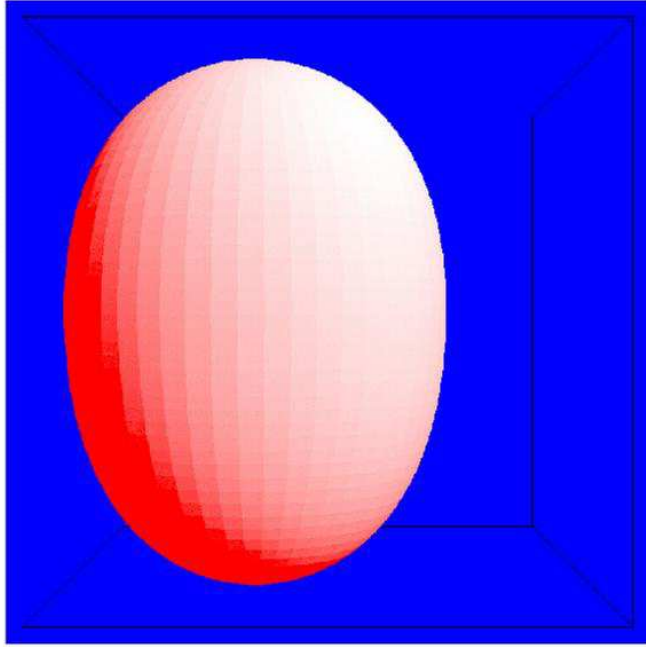


Fig. 12. Model of GW 46.4+5.5. The parameters are $t_{\text{age}}=0.5 \cdot 10^7$ yr, $\Delta t = 0.001 \cdot 10^7$ yr, $t_7^{\text{burst}} = 0.5$, $N^* = 150$, $z_{\text{OB}}=100$ pc, and $E_{51}=1$. The three Eulerian angles characterising the point of view of the observer are $\Phi = 0^\circ$, $\Theta = 90^\circ$ and $\Psi = 0^\circ$.

observation of HI gas associated with GW 46.4+5 (Hartmann, Burton 1997; Kim , Koo 2000) reveals that the super-shell has an expansion velocity of $V_{\text{exp}} \approx 15 \text{ km s}^{-1}$ (Kim , Koo 2000). In order to see how our model matches the observations, the instantaneous radial velocities are computed in each direction. A certain number of random points are then generated on the theoretical surface of expansion. The relative velocity of each point is computed by using the method of bilinear interpolation on the four grid points that surround the selected latitude and longitude (Press et al. 1992).

Our model gives radial velocities of, V_{theo} , $31 \text{ km s}^{-1} \leq V_{\text{theo}} \leq 71 \text{ km s}^{-1}$ ($27 \text{ km s}^{-1} \leq V_{\text{theo}} \leq 66 \text{ km s}^{-1}$ with the Euler process) and a map of the expansion velocity is given in figure 14, from which it is possible to visualise the differences in the expansion velocities among the various regions.

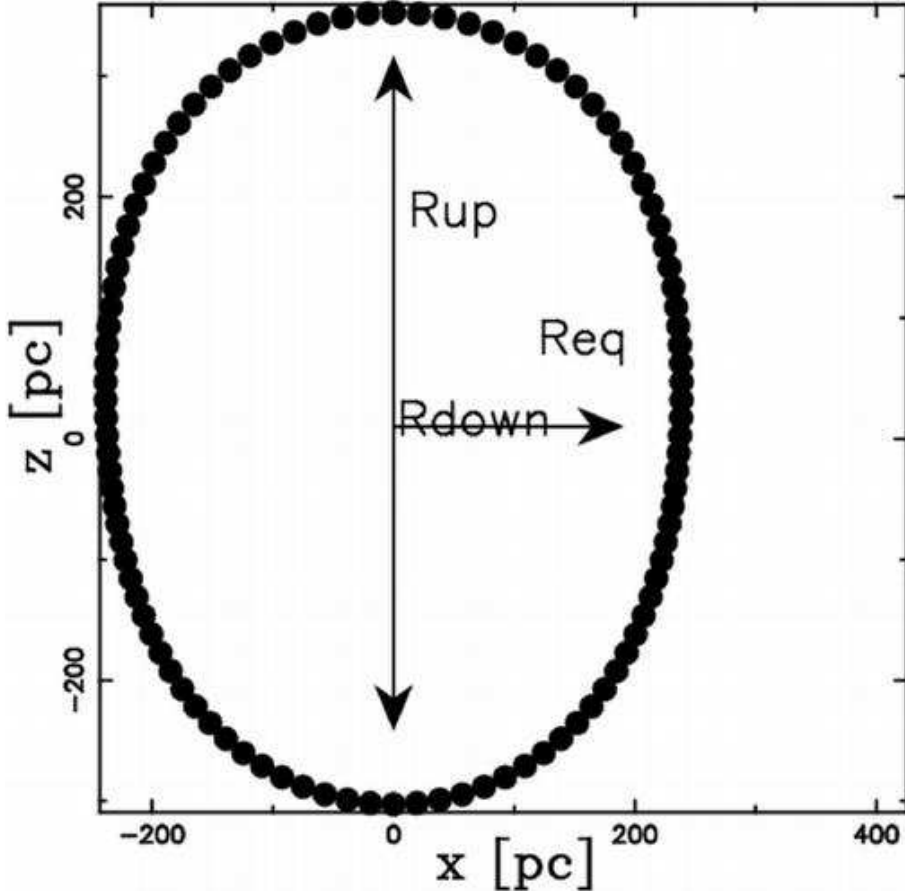


Fig. 13. Section of the superbubble on the x - z plane when the physical parameters are the same as in figure 12.

Perhaps it is useful to map the velocity (V_{theo}^p) in the y -direction,

$$V_{\text{theo}}^p = v(\theta, \phi) \cdot \sin(\theta) \cdot (\sin \phi). \quad (55)$$

This is the velocity measured along the line of sight when an observer stands in front of the super-bubble; θ and ϕ are defined in subsection 2.2. The structure of the projected velocity, V_{theo}^p , is mapped in figure 15 by using different colours; the range is $0 \text{ km s}^{-1} \leq V_{\text{theo}}^p \leq 36 \text{ km s}^{-1}$ ($0 \text{ km s}^{-1} \leq V_{\text{theo}}^p \leq 32 \text{ km s}^{-1}$ with the Euler process) and the averaged projected velocity is $\approx 20 \text{ km s}^{-1}$ ($\approx 17.6 \text{ km s}^{-1}$ with the Euler process), a value that is greater by $\approx 5 \text{ km s}^{-1}$ ($\approx 2.6 \text{ km s}^{-1}$ with the Euler process) than the already mentioned observed expansion velocity, $V_{\text{exp}} = 15 \text{ km s}^{-1}$.

As is evident from the map in figure 15, the projected velocity of expansion is not uniform over all of the shell's surface, but it is greater in the central region in comparison to the external region. In this particular case of an egg-shape, we observe a nearly circular region connected with the maximum velocities in the upper part of the shell. It is therefore possible to speak of egg-shape appearances in the Cartesian physical coordinates and spherical-appearances in the projected maximum velocity.

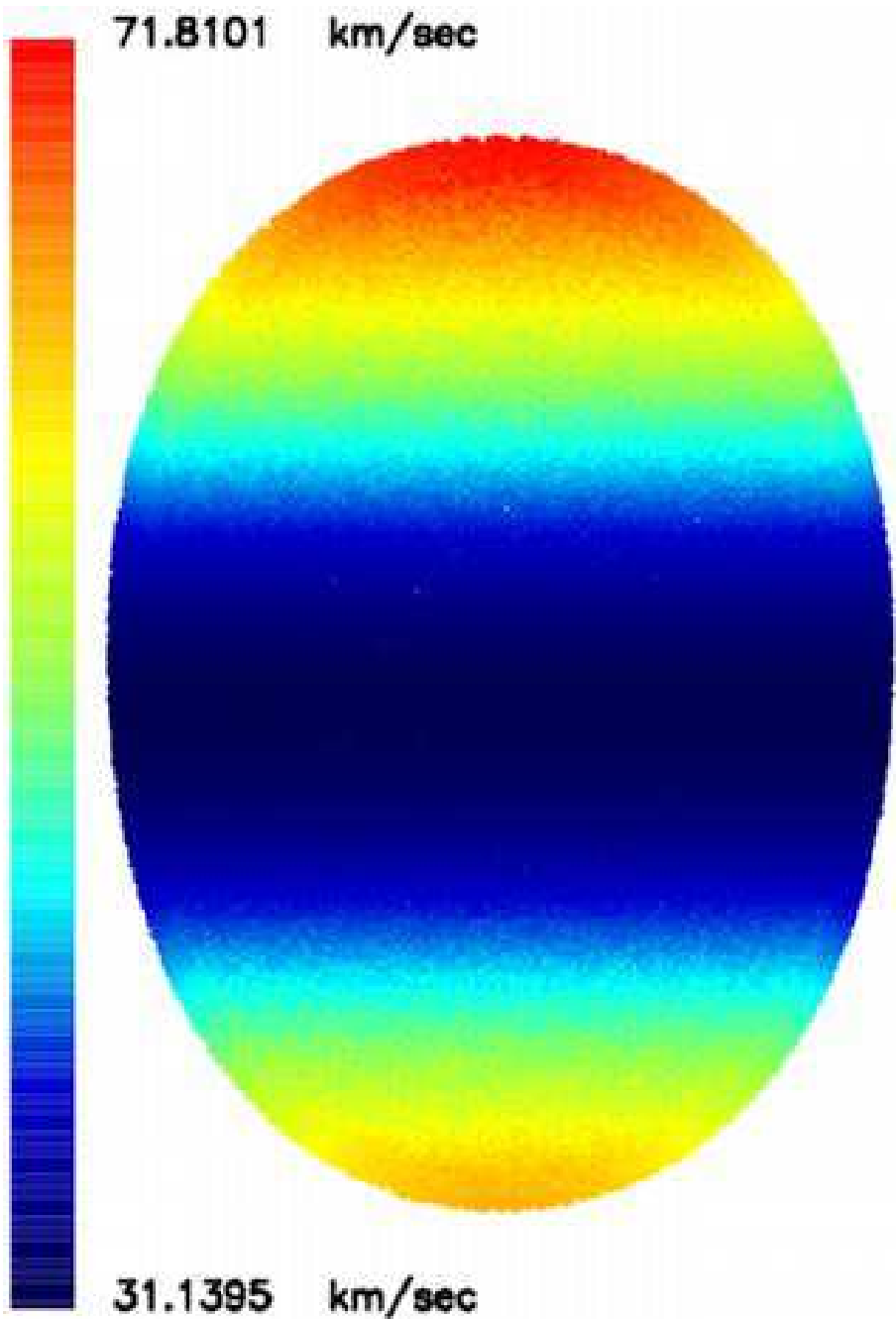


Fig. 14. Map of the expansion velocity relative to a simulation of GW 46.4+5.5 when 190000 random points are selected on the surface. The physical parameters are the same as in figure 12 and the three Eulerian angles characterising the point of view of the observer are $\Phi = 0^\circ$, $\Theta = 90^\circ$, and $\Psi = 0^\circ$.

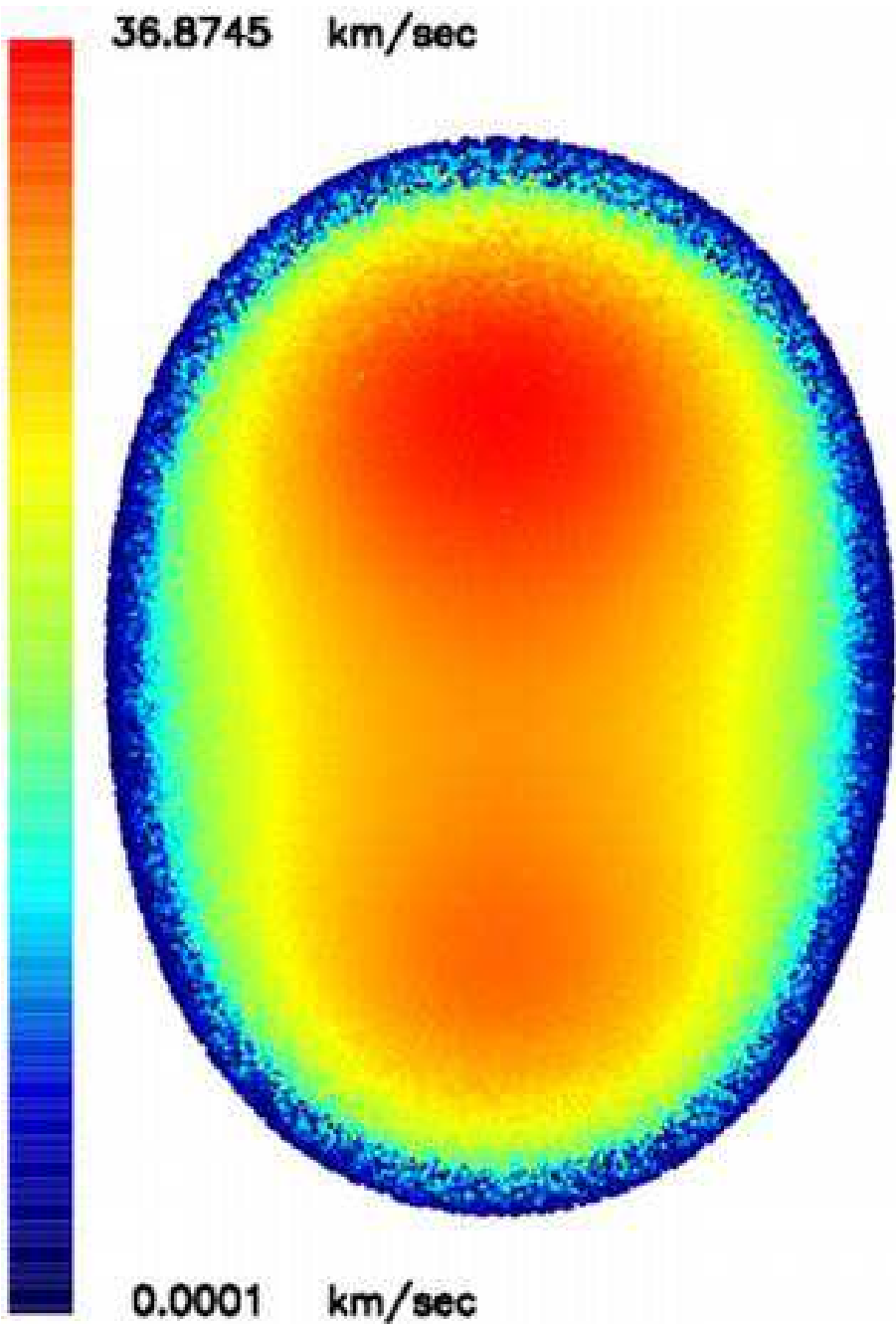


Fig. 15. Map of the velocity along the line of sight, V_{theo}^p , relative to a simulation of GW 46.4+5.5 when 190000 random points are selected on the surface. The physical parameters are the same as in figure 15.

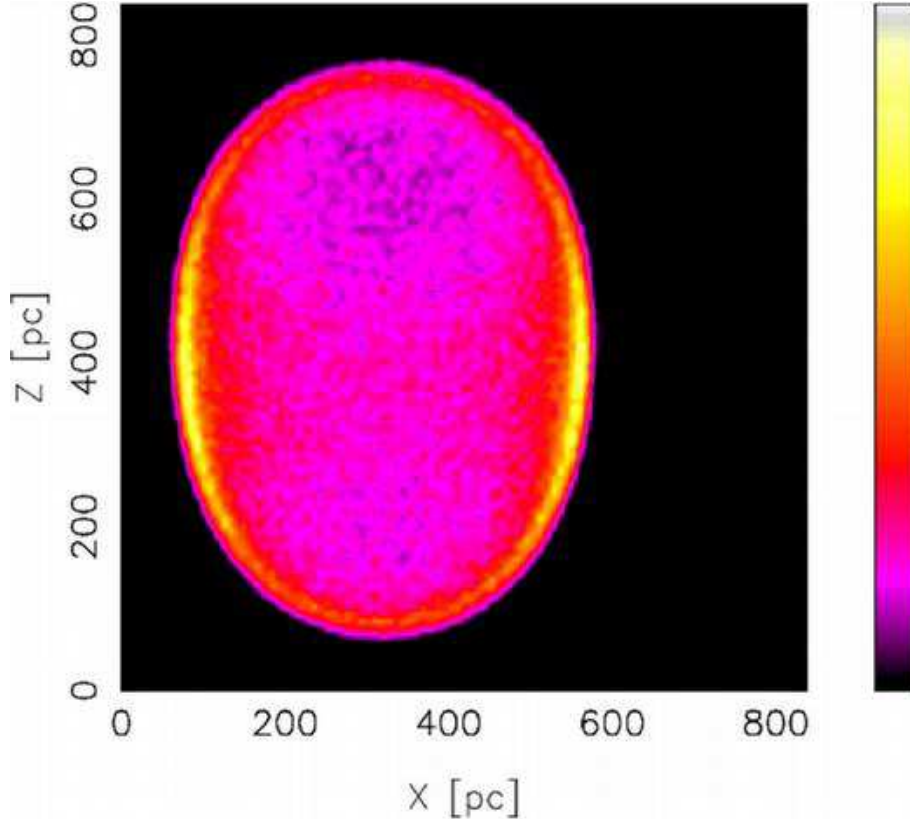


Fig. 16. Number of particles, N^p , along the line of sight relative to the simulation of GW 46.4+5.5 when NDIM=101. The other parameters are as in figure 15.

Another way of presenting the results is through a ring-enhancement due to the law of e.m. emission in the external layer (see appendix 1). The projected number of particles $N^p(i,j)$, is then mapped using colour-coding contours (figure 16); the density enhancement in the ring region is evident from a visual inspection of this simulated map.

Upon adopting formula (31), it is possible to map the field of temperature of the super-shell associated with GW 46.4+5.5 (see figure 17).

The effect of galactic rotation on the shape of the superbubble is shown in figure 18 where a circle is transformed into an ellipse.

4.2. GSH 238

The physical parameters concerning GSH 238, as deduced in Heiles (1998), are reported in table 4. The total energy is obtained based on a model derived by Heiles 1979 and the kinematic age is derived from approximate arguments. Once again, in order to obtain $E_{\text{tot}} = 34 \cdot 10^{51} \text{ erg}$ [see formula (29)] and $t^{\text{burst}} = 0.015 \cdot 10^7 \text{ yr}$, we have inserted $N^* = 11300$.

The efficiency over 50+1 directions computed with formula (54) of a section x - y when $z=0$, is $\epsilon_{\text{obs}} = 58.4\%$. The 2D cut at $z=0$ of the superbubble can be visualised in figure 19. Our model gives a radial velocity at $z=0$ $V_{\text{theo}} = 6 \text{ km s}^{-1}$ against the observed 8 km s^{-1} at $b=0$.

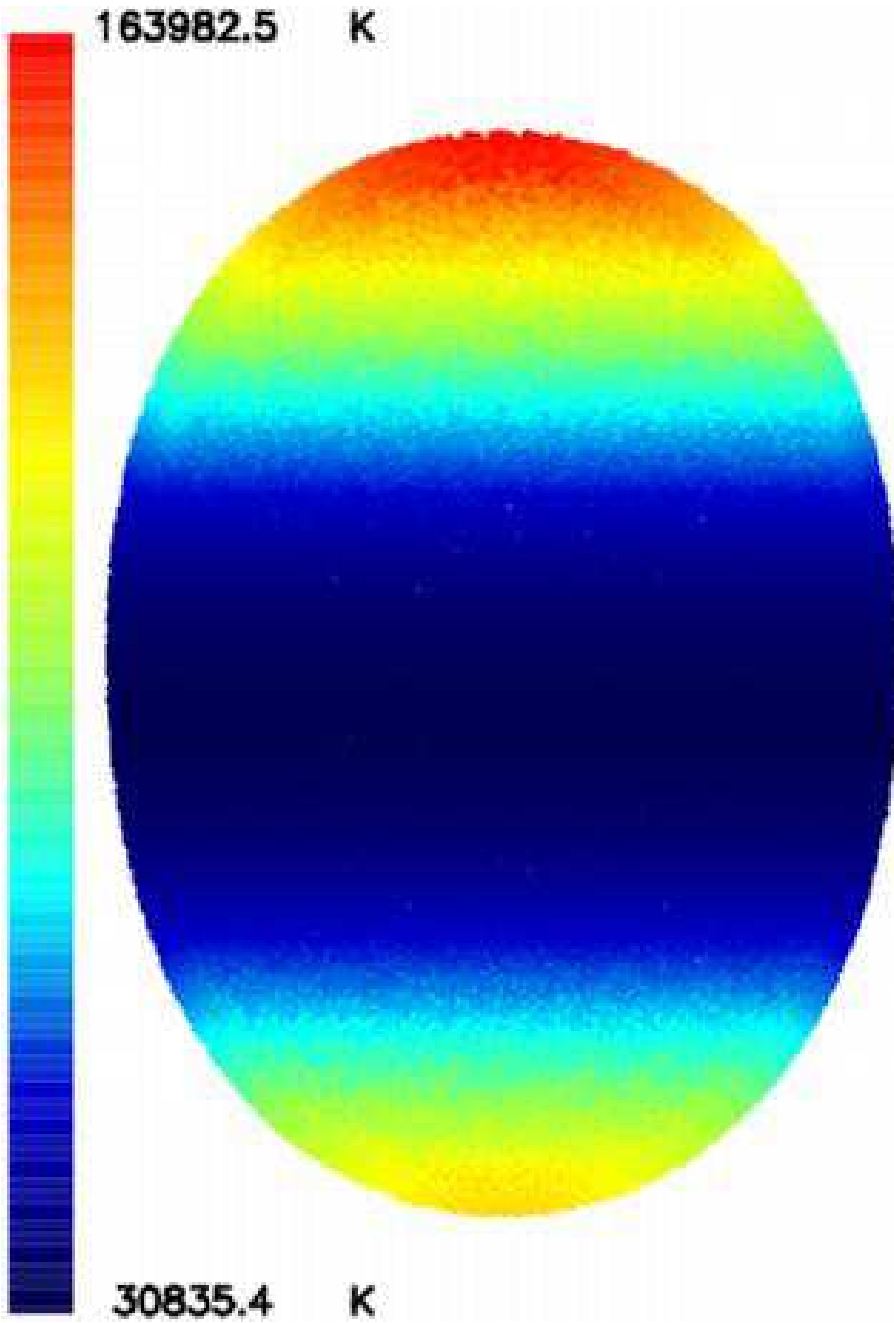


Fig. 17. Map of the temperature relative to the simulation of the supershell associated with GW 46.4+5.5; the other parameters are the same as in figure 14.

Table 4. Data of the super-shell associated with GSH 238.

Size (pc ²)	440 · 1100 at b=0
Expansion velocity (km s ⁻¹)	8
Age (10 ⁷ yr)	2.1
Total energy (10 ⁵¹ erg)	34

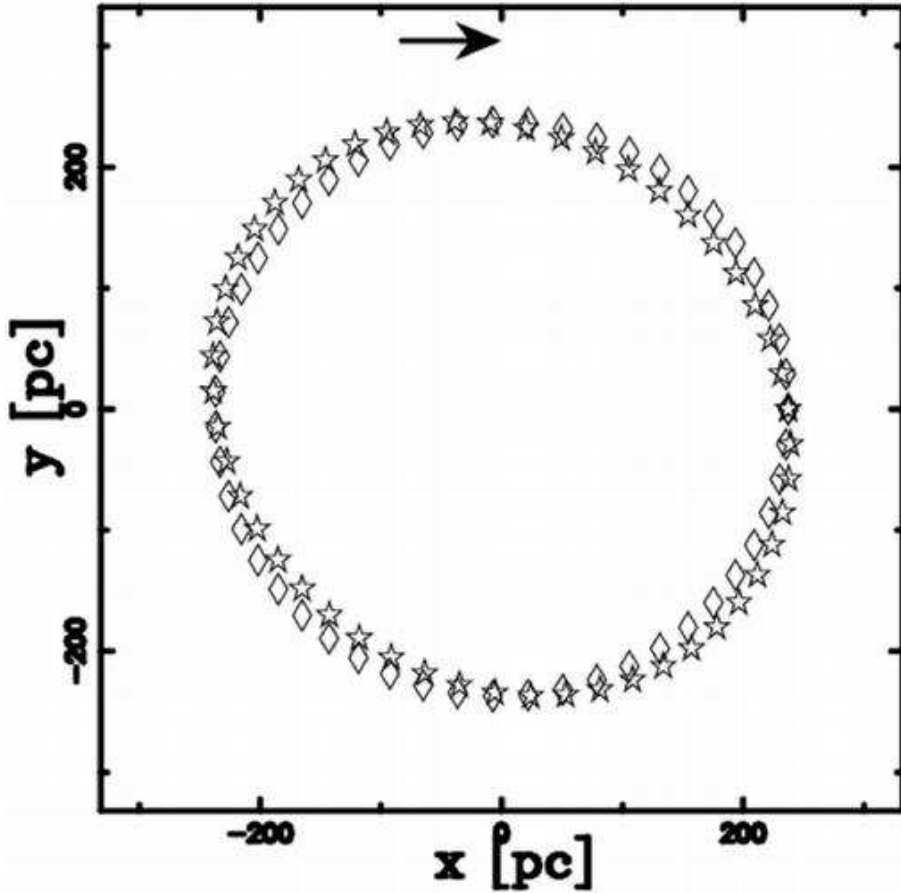


Fig. 18. Circular and rotation-distorted sections of the superbubble on the x - y plane, denoted by $z=z_{\text{OB}}$. The physical parameters are the same as in figure 12; the rhombi represent the circular section and the stars the rotation-distorted section; the Galaxy direction of rotation is also shown.

5. Collective Effects

It should be remembered that the worms have an average linear extent in the z direction of 150 pc and a median width of 70 pc; the maximum extension that can be reached in the z -direction is ≈ 1 kpc (Koo et al. 1992). These observations can be simulated by introducing a coupling between the percolation network reviewed in appendix 2 and the explosion *model* described in section 2. The percolation offers:

1. The Cartesian coordinates of the explosions in the galactic plane that follow the grand-designed spiral galaxies.
2. The times of the clusters vary between 10^7 yr and 10^8 yr. This cluster age divided by 4 can be identified with t_{age} , the age of the superbubble. With this last choice, the maximum t_{age} is $2.5 \cdot 10^7$ yr, according to the age of GSH 238, the oldest super-shell analysed here. In other words, the time sequence of the clusters (1,2,...,10 $\cdot 10^7$ yr) is converted in the following age sequence of the super-shells (0.25,0.5,...,2.5 $\cdot 10^7$ yr). This choice fixes the maximum altitude reached by the super-shells in ≈ 600 pc.

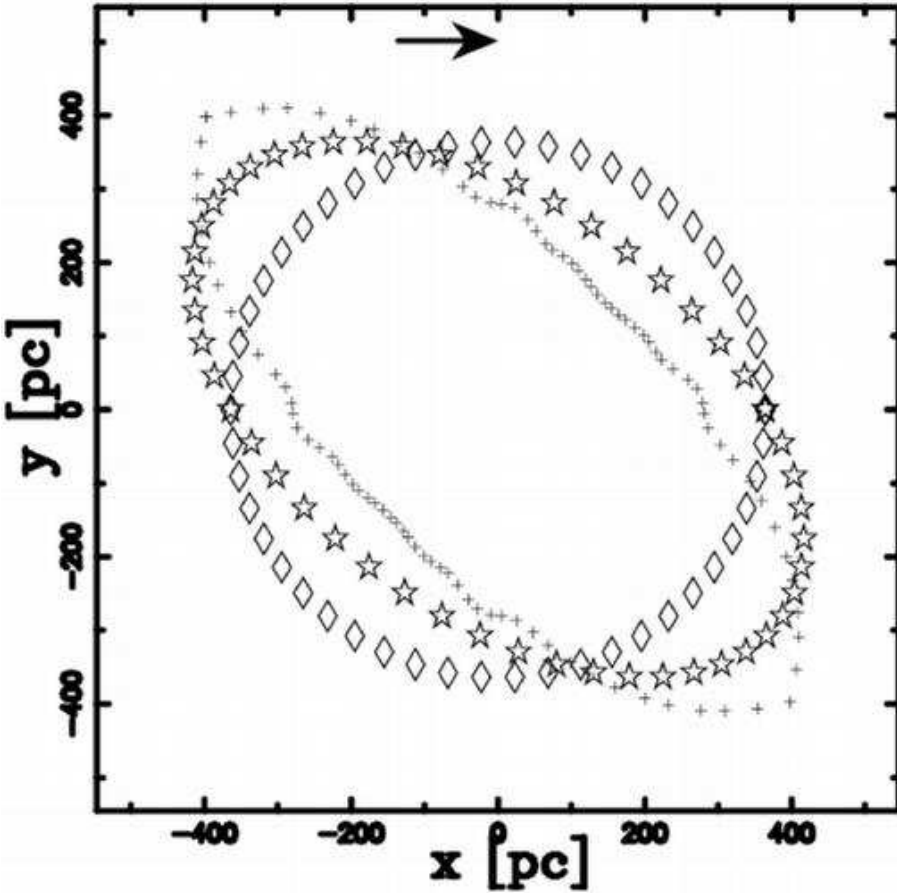


Fig. 19. Rhombi represent the circular section; the stars, the rotation-distorted section; and the small crosses, the observed data of GSH 238 at $b = 0$ (our $z=0$) as extracted from figure 8 of Heiles (1998). The Galaxy direction of rotation is also shown. The parameters are $t_{\text{age}}=2.1 \cdot 10^7$ yr, $\Delta t = 0.001 \cdot 10^7$ yr, $t_7^{\text{burst}} = 0.015$, $N^* = 11300$, $z_{\text{OB}}=0$ pc, and $E_{51}=1$.

In order to test the suggested coupling between superbubbles and the percolation the distance of 200 pc, which the explosions should cover in one time step, 10^7 yr was inserted in equation (26), in order to trigger new cluster formations.

Upon adopting the standard values of $n_0 = 0.4 \text{ particles cm}^{-3}$, $E_0=1$ and $N^*=150$, we obtain $t_7^{\text{burst}}=0.035$, a value that seems to be in agreement with our previous assumption in which the bursting phase is lower than the age of the superbubble. A typical percolation run is shown in figure 20 for a face-on galaxy. The galactic rotation is considered in all the simulations discussed in this section.

5.1. Few Superbubbles

In order to visualise a few explosions of coordinates X and Y , only those clusters comprised between $\text{XMIN}[\text{pc}] \Leftrightarrow \text{XMAX}[\text{pc}]$ and $\text{YMIN}[\text{pc}] \Leftrightarrow \text{YMAX}[\text{pc}]$ should be selected. The distance z_{OB} from the galactic plane of the clusters is allowed to randomly vary between -100 pc and 100 pc, which is the size of the active regions. A typical example of this network of

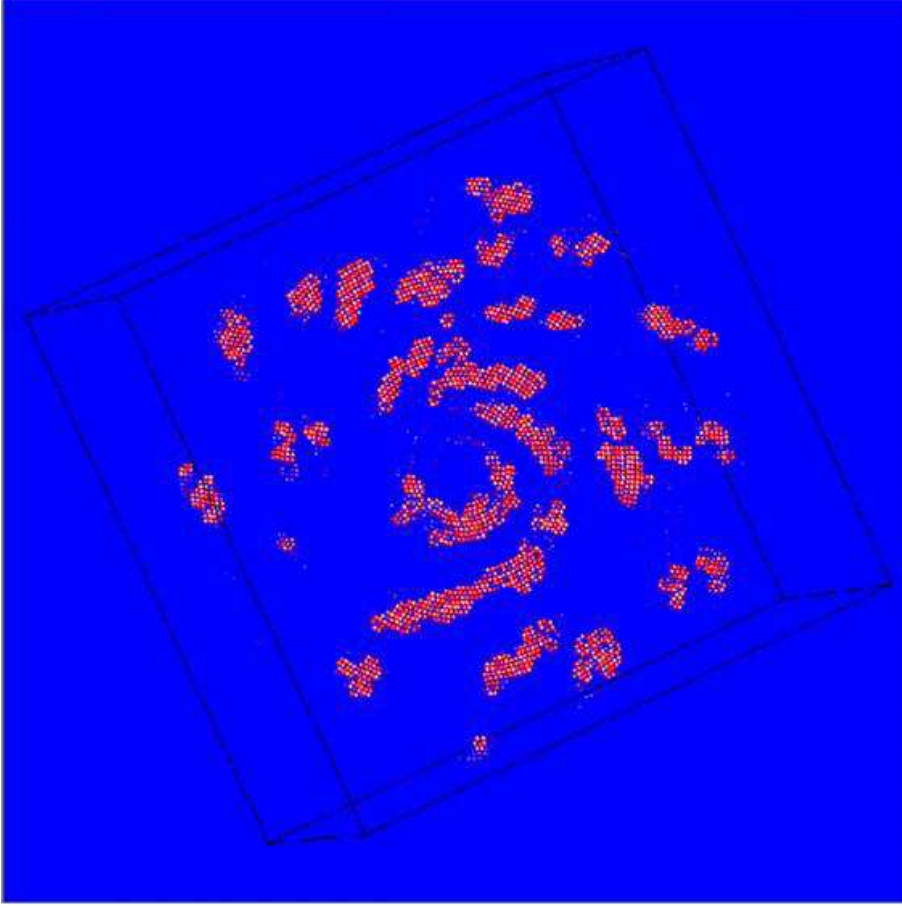


Fig. 20. Simulation of spiral galaxy S_b by adopting the theory and the parameters of appendix 2. The clusters are represented by spheres of decreasing radius with increasing age. The three Eulerian angles characterising the point of view of the observer are $\Phi = 25^\circ$, $\Theta = 75^\circ$, and $\Psi = 25^\circ$.

multi-explosions is shown in figure 21 through the algorithm that counts the number of particles along the line of sight; the selected boundaries are marked on plots and the appearance of the rings is evident.

The superbubbles can also be visualised when the observer is situated in front of the galaxy plane (see figure 22). The effect of shape distortion due to formula (35) is evident.

5.2. The Galactic Plane

In order to simulate the structure of the galactic plane, the same basic parameters as in figure 20 can be chosen, but now the superbubbles are drawn on an equal-area Aitoff projection. In particular, a certain number of clusters will be selected through a random process according to the following formula:

$$\text{selected clusters} = p_{\text{select}} \cdot \text{number of clusters from percolation}, \quad (56)$$

where p_{select} has a probability lower than one. The final result of the simulation is reported in figure 23.

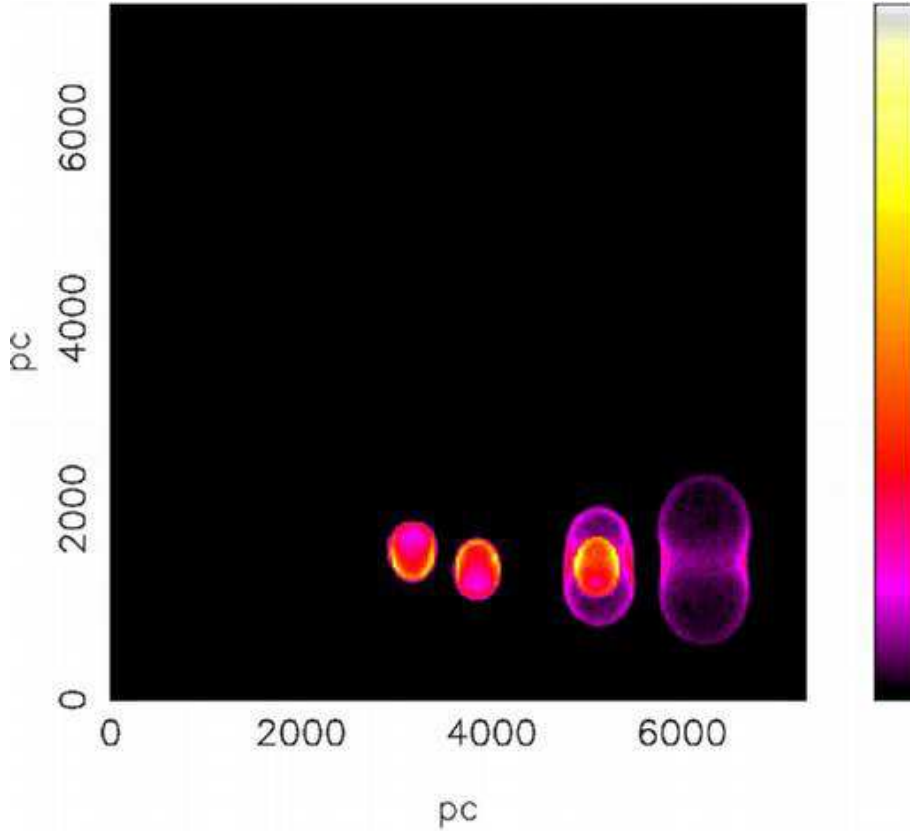


Fig. 21. Number of particles, N^p , along the line of sight relative to the network of the explosions when $NDIM=200$ and the galaxy is situated edge on. The boundaries of the box are $XMIN=YMIN=-8000$ pc, $XMAX=YMAX=-4000$ pc; 5 clusters were selected and each superbubble had 40000 random points on it's surface. The parameters were $\Delta t = 0.01 \cdot 10^7$ yr, $t_7^{\text{burst}} = 0.2$, and $N^* = 50$.

We can also visualise the structure of the superbubbles as seen from an observer situated outside the Galaxy; the spiral structure arising from the ensemble of the shells is evident (see figure 24). The elliptical shape of the superbubble, according to formula (35), is a function of both the age and the distance from the center. The distortion also follows the same inclination of the arms.

6. Conclusions

The expansion of a super-bubble in the ISM belonging to our galaxy can be simulated by applying Newton's second law to different pyramidal sectors. The following results were achieved:

1. Characteristic structures, such as hourglass-shapes, vertical walls and V-shapes, could be obtained by varying the basic parameters, which are the bursting phase and the time over which the phenomena are followed.
2. Single objects, like the super-shells associated with GW 46.4+5 and GSH 238 were simulated with an efficiency $\epsilon_{\text{obs}} \approx 68\%$ and $\epsilon_{\text{obs}} \approx 58\%$, respectively.

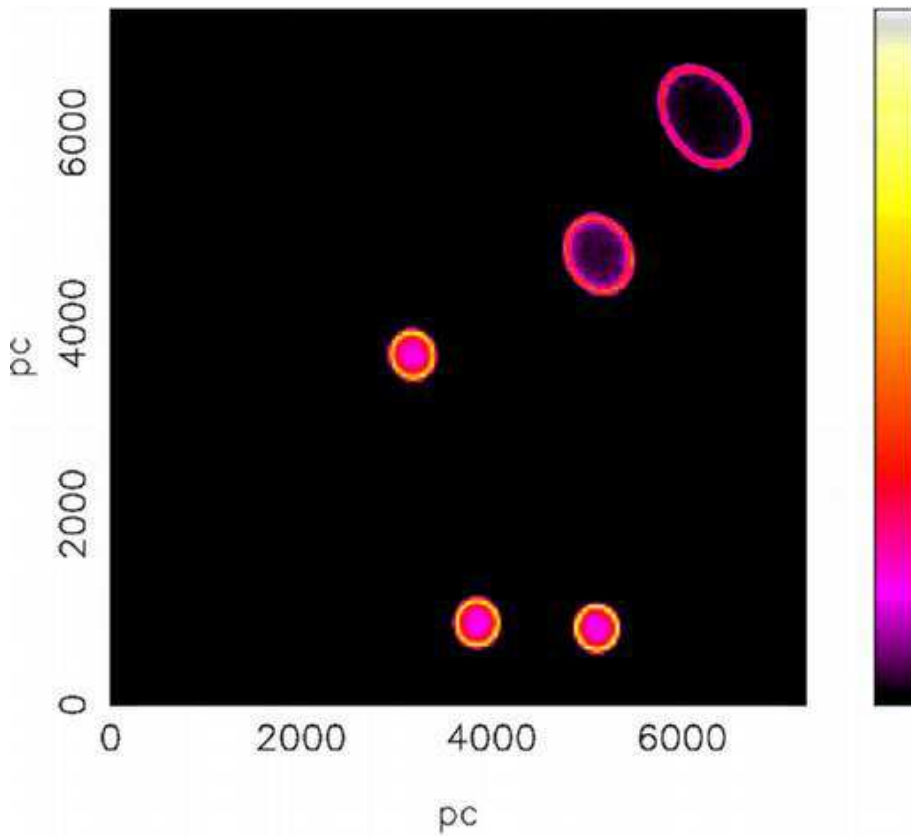


Fig. 22. Same as figure 21, but when the galaxy is situated face on.

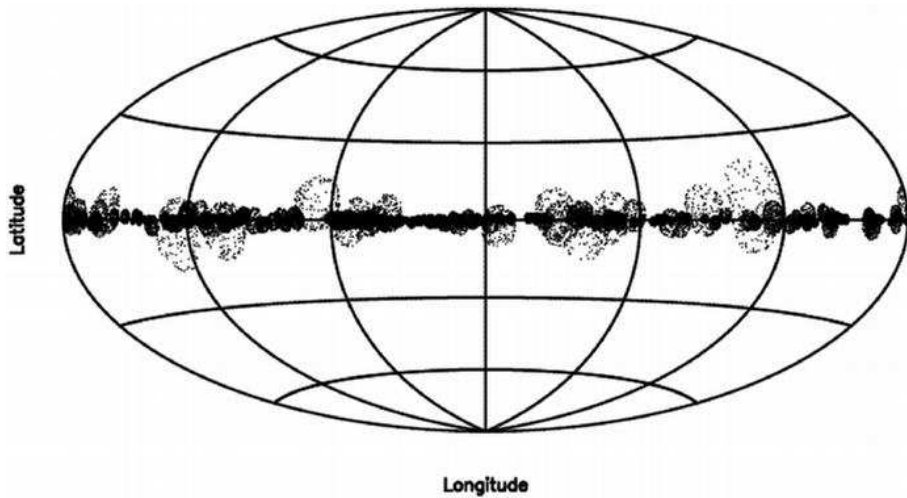


Fig. 23. Structure of the galactic plane in the Hammer-Aitoff projection, as resulting from the superbubble/percolation network. The value of p_{select} is 0.08, corresponding to 260 selected clusters. The parameters were $\Delta t = 0.01 \cdot 10^7$ yr, $t_7^{\text{burst}} = 0.5$, $N^* = 100$ and each superbubble had 200 random points on its surface.

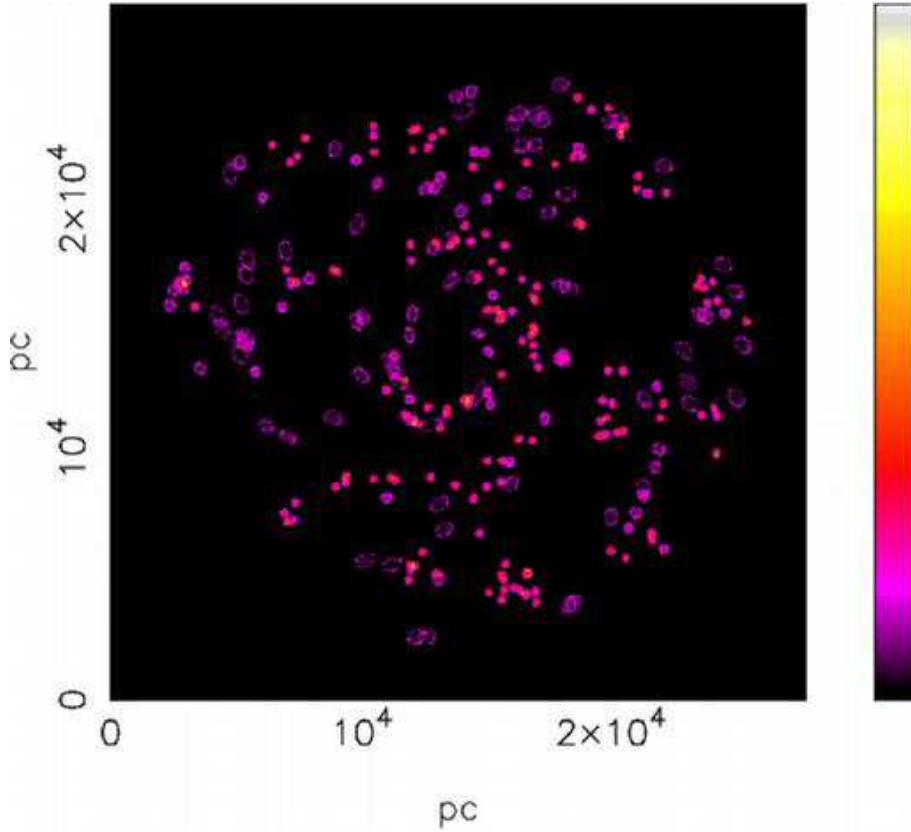


Fig. 24. Number of particles, N^p , along the line of sight relative to the network of the explosions when the galaxy is face on. Physical parameters were as in figure 23 and NDIM= 401.

3. The network of many explosions that originate from the galactic plane could be tentatively simulated.

Some problems are still unsolved:

1. The results were obtained by using a standard law concerning the dependence of the ISM on the distance from the galactic plane, z . Perhaps a more refined treatment of the HI thin disk will change the obtained morphologies.
2. Recent maps based on measurements of NaI absorption in the surroundings of the Local Bubble suggest the existence of narrow tunnels (Welsh et al. 2003). Can a tunnel be explained by the interaction of a super-bubble arising from the galactic plane (GSH 238) with a smaller interstellar bubble (the Local Bubble) ?

Appendix 1. The Density Projection Algorithm

Consider a shell within two concentric spheres with radii R and $R + \Delta R$. The total intensity of thermal e.m. radiation, when absorption and scattering are neglected, is proportional to the following parameter (chosen among others): $I \propto l$, where l is the dimension of the radiating region along the line of sight; I_{ring} and I_{center} denote, respectively, the intensity along

the ring and along the center. The length of the emitting region when the line of sight touches the inner shell is

$$l_{\text{ring}} = 2\sqrt{(R + \Delta R)^2 - R^2}. \quad (\text{A1})$$

Conversely, when the line of sight is aligned with the center of the two shells the emitting length is

$$l_{\text{center}} = 2\Delta R. \quad (\text{A2})$$

We briefly remember that on applying mass conservation to a region of radius R before and after an explosion and the junction condition concerning the density, the following formula concerning the depth of the expanding layer is obtained:

$$\frac{\Delta R}{R} = \frac{\gamma - 1}{\gamma + 1} \frac{1}{3} = \frac{1}{12}, \quad (\text{A3})$$

where $\gamma = \frac{5}{3}$ (see Deeming, Bowers 1984). By using a little algebra, we find

$$\frac{l_{\text{ring}}}{l_{\text{center}}} = 5. \quad (\text{A4})$$

This argument is easily generalised in the case of $\Delta R = R/n_t$ where n_t is an integer greater than 12 :

$$\frac{l_{\text{ring}}}{l_{\text{center}}} \approx \sqrt{2n_t} \text{ when } \Delta R = R/n_t. \quad (\text{A5})$$

Therefore, the ratio $\frac{I_{\text{ring}}}{I_{\text{center}}} = \frac{l_{\text{ring}}}{l_{\text{center}}}$ can be called "the center darkening law", and says that the center of the superbubble should have a lower emergent intensity than the shell region (the limb). We point out that on the expanding surface of the superbubble there is a certain value of the intensity [for example, 30 $\frac{\text{MJy}}{\text{sr}}$ in the band of $100 \mu\text{m}$ (far-IR) (see figure 1 (gray-scale intensity) in (Kim, Koo 2000))]. The intensity at the center of the superbubble is theoretically predicted to be approximately five times lower than that of the ring (therefore, 5 $\frac{\text{MJy}}{\text{sr}}$). This argument was applied to our superbubble by plotting the density of random particles projected on the sky. In order to implement such a projection, we first computed the number of random elements ($N(i, j, k)$) that fall in a little cube of volume $\text{side}^3/\text{NDIM}^3$ where side is considered to be the length of the cube that encloses the superbubble, and NDIM the number of considered pixels. We then sum over one index, for example k , in order to obtain the elements $N^p(i, j)$ that fall in a given area $= \frac{\text{side}^2}{\text{NDIM}^2}$. The already described algorithm can be considered a simulation of the number of particles that are being emitted on the line of sight.

Appendix 2. Percolation and spiral galaxies

The appearance of arms can be simulated through the percolation theory (Seiden, Gerola 1979; Seiden 1983; Schulman, Seiden 1986; Seiden, Schulman 1990); here, a previous model (Zaninetti 1988) will be slightly modified. The fundamental hypotheses and the parameters adopted in the simulation are now reviewed:

1. The motion of gas on the galactic plane has a constant rotational velocity, named V_G (in the case of spiral type Sb 218 kms^{-1}). Here the velocity, V_G , is expressed in 200 kms^{-1} units and will therefore be $V_G = 1.09$.
2. The polar simulation array made by rings and cells has a radius $R_G = 12 \text{ kpc}$. The number of rings, (60), is the multiplication together of R_G and the number of rings for each kpc, named nring/kpc , which in our case is five. Every ring is then made up of many *cells*, each one with a size on the order of the galactic thickness, $\approx 0.2 \text{ kpc}$. The parameter nring/kpc can also be found by dividing 1kpc by the approximate cell's size.
3. The global number of cells, 11121, multiplied by the probability of spontaneous new cluster formation, p_{sp} (for example 0.01), allows the process to start (with the previous parameters, 111 new clusters were generated). Each one of these sources has six new surroundings that are labelled for each ring.
4. In order to better simulate the decrease of the gas density along the radius, a stimulated probability of forming new clusters with a linear dependence by the radius, $p_{st} = a + bR$, was chosen. The values a and b are found by fixing $prmax$ (for example 0.18), the stimulated probability at the outer ring, and $prmin$ (for example 0.24) in the inner ring; of course, $prmin \geq prmax$. This approach is surprisingly similar to the introduction of an anisotropic probability distribution in order to better simulate certain classes of spirals (Jungwiert, Palous 1994).
5. Now, new sources are selected in each ring based on the hypothesis of different stimulated probabilities. A rotation curve is imposed so that the array rotates in the same manner as the galaxy. The procedure repeats itself n times (100); we denote this by t_G the age of the simulation, $100 \cdot 10^7 \text{ yr}$ being 10^7 yr , the astrophysical counterpart of one time step.
6. In order to prevent catastrophic growth, the process is stopped when the number of surroundings is greater than max (1000) and restarts by spontaneous probability.
7. The final number of active cells (3258) is plotted with the size, which decreases linearly with the cluster age. In other words, the young cluster are bigger than the old ones. Only ten cluster ages are shown; only cells with an age of less than life (in our case $10 \cdot 10^7 \text{ yr}$) are selected. A more deterministic approach has been followed by Palous et al (1994), where a model that connects the energy injection by star formation with the resulting interstellar structures in a differentially rotating disc has been introduced.

References

Basu, S., Johnstone, D., & Martin, P. G. 1999, ApJ, 516, 843
 Begelman, M. C. ,& Li, Z.-Y. 1992, ApJ, 397, 187
 Bisnovatyi-Kogan, G. S. ,& Silich, S. A. 1995, Rev. Mod. Phys., 67, 661
 Boulares, A. ,& Cox, D. P. 1990, ApJ, 365, 544

Deeming, T.,& Bowers, R.L. 1984, *Astrophysics II: Interstellar Matter and Galaxies*, (Boston: Jones & Bartlett Pub)

Dickey, J.M. ,& Lockman, F.J. 1990, *ARA&A*, 28, 215

Ferriere, K. M., Mac Low, M., & Zweibel, E. G. 1991, *ApJ*, 375, 239.

Franco, J., Kim, J., Alfaro, E. J., & Hong, S. S. 2002, *ApJ*, 570, 647

Hartmann,D. ,& Burton, W.B. 1997, *Atlas of Galactic Neutral Hydrogen* (Cambridge: Cambridge University Press)

Heiles, C. 1979, *ApJ*, 229, 533

Heiles, C. 1998, *ApJ*, 498, 689

Igumenshchev, L.V.,Shustov, B.M. ,& Tutukov, A.V. 1990, *A&A* , 234, 396

Jungwiert, B. ,& Palous,J. 1994, *A&A*, 287,55

Kamaya, H. 1998, *ApJL*, 493, L95

k Kim, J., Franco, J., Hong, S. S., Santillán, A., & Martos, M. A. 2000, *ApJ*, 531, 873

Kim,K.T. ,& Koo,B. C. 2000, *ApJ* , 529, 229

Koo, B. C. ,& McKee, C. F. 1990, *ApJ*, 354, 513

Koo,B.C.,Heiles,C. ,& Reach,W.T 1992, *ApJ* , 390 , 108

Lockman, F.J. 1984, *ApJ* , 283, 90

Mac Low, M.-M. ,& McCray, R. 1988, *ApJ*, 324, 776.

MacLow, M.-M. , McCray, R. ,& Norman,M.L. 1989, *ApJ* , 337,141

McCray, R. 1987, in *Spectroscopy of Astrophysical Plasmas*, ed. A. Dalgarno A. & D. Layzer (Cambridge: Cambridge University Press) 271

McCray, R. ,& Kafatos , M. 1987, *ApJ* , 317,190

McKee C.F., 1987, in *Spectroscopy of Astrophysical Plasmas*, ed. A. Dalgarno A. & D. Layzer (Cambridge: Cambridge University Press) 226

Moreno, E., Alfaro, E. J., & Franco, J. 1999, *ApJ*, 522, 276

Palous, J., Franco, J., ,& Tenorio-Tagle, G. 1990, *A&A*, 227, 175

Palous, J., Tenorio-Tagle, G., & Franco, J. 1994, *MNRAS*, 270, 75

Pikel'ner, S. B. 1968, *Astrophys. Lett.*, 2, 97

Press,W. H. , Teukolsky, S. A. , Vetterling, W. T. , & Flannery, B. P., 1992 *Numerical Recipes in Fortran* , second edition (Cambridge: Cambridge University Press) , 117

Puche,D.,Westpfahl,D.,Brinks,E. ,& Roy,J.-R. 1992, *AJ* , 103, 1841

Santillán, A., Franco, J., Martos, M., & Kim, J. 1999, *ApJ*, 515, 657

Schulman, L. S. ,& Seiden, P. E. 1986, *Science*, 233, 425

Seiden, P. E. 1983, *ApJ*, 266, 555

Seiden, P. E. ,& Gerola, H. 1979, *ApJ*, 233, 56

Seiden,P.E. ,& Schulman,L.S. 1990, *Advances in Physics* , 39,1

Silich, S. A. 1992, *Ap&SS*, 195, 317

Silich, S. A., Franco, J., Palous, J. ,& Tenorio-Tagle, G. 1996, *ApJ*, 468, 722

Silich, S. A., Mashchenko, S.Y. , Tenorio-Tagle, G., ,& Franco, J. 1996, *MNRAS*, 280, 711

Stone, J.M. ,& Norman, M. L. 1992, *ApJS*, 80, 753

Tenorio-Tagle, G. ,& Bodenheimer, P. 1988, *ARA&A*, 26, 145

Tomisaka, K. 1992, PASJ, 44, 177.

Tomisaka, K. 1998, MNRAS, 298, 797.

Tomisaka,K. ,& Ikeuchi,S. 1986, PASJ, 38,697

Walter, F., Kerp, J., Duric, N., Brinks, E. ,& Klein, U. 1998, ApJ, 502, L143

Weaver, R., McCray, R., Castor, J., Shapiro, P., ,& Moore, R. 1977 , ApJ, 218, 377

Welsh, B. Y., Lallement, R., Vergely, J. L., Crifo, F., & Sfeir, D. 2003, BAAS, 202,53

Wouterloot, J. G. A., Brand, J., Burton, W. B., & Kwee, K. K. 1990, A&A, 230, 21

Zaninetti, L. 1988, A&A , 190, 17